

# Beyond the Microscale: Advances in Surface Nanopatterning by Laser-Driven Self-Organization

Anthony Nakhoul<sup>1,2</sup> | Jean-Philippe Colombier<sup>1\*</sup>

<sup>1</sup>UJM-Saint Etienne, CNRS, Laboratoire Hubert Curien UMR 5516, Institute of Optics Graduate School, University of Lyon, St-Etienne F-42023, France

<sup>2</sup>Mines Saint-Etienne, CNRS, Centre SMS, Laboratoire Georges Friedel, University of Lyon, UMR5307, St-Etienne F-42023, France

## Correspondence

Dr. J-P. Colombier  
Univ Lyon, UJM-Saint-Etienne, CNRS,  
IOGS, Laboratoire Hubert Curien  
UMR5516, F-42023  
St-Etienne, France  
Email:  
jean.philippe.colombier@univ-st-etienne.fr

## Funding information

This work has been funded by a public grant from the French National Research Agency (ANR) under the “France 2030” investment plan, which has the reference EUR MANUTECH SLEIGHT-ANR-17-EURE-0026.

Designing complex local properties that seamlessly integrate efficient functions into processed materials presents a formidable challenge. A promising solution has emerged in the form of ultrafast laser-surface structuring. Through time-controlled polarization ultrafast irradiation at the picosecond timescale, spontaneous self-organization of surfaces can be induced. The thermal gradient length scale unfolds on the micro- and nanoscale, instigating thermoconvection that leads to structured surfaces upon quenching. Convective instabilities dynamically shape intricate yet self-regulated periodic relief structures. The ability to achieve laser-induced self-organization in both surface dimensions holds immense scientific importance, as it unlocks the potential to create uniform periodic 2D patterns by harnessing the inherent regulation of nonlinear dynamics processes in fluids. This comprehensive review explores recent advances in understanding and leveraging ultrafast laser-induced self-organization for precise patterning across versatile scales and applications. The insights herein hold the potential to drive significant advancements in nanoscale manufacturing through 2D laser-induced periodic surface structures.

## KEYWORDS

2D-LIPSS, self-organization, surface engineering, nanostructured surfaces, ultrafast laser.

## 1 | INTRODUCTION

The remarkable progress in manufacturing, energy conversion, and transportation heavily relies on the precise manipulation of material properties at the nanoscale. Creating regularly nanostructured materials presents a tremendous potential for revolutionizing our technological environment by engineering artificial materials with unprecedented surface properties. Exploring extreme surface manufacturing with increasingly smaller sizes and higher precision is required to meet the demands of nano-optics [1], heat conversion [2], and nanofluidic [3]. Ultrafast laser structuring has emerged as a potentially greener and more cost-effective technique for advanced surface functionalization by a direct irradiation process compared to traditional methods like chemical etching and mechanical structuring, since it enables highly enhanced flexibility and minimizes thermal loss by localizing light energy [4, 5].

Close to the modification energy threshold of most materials, it is possible to generate a periodic alignment of surface ripples, commonly known as Laser-Induced Periodic Surface Structures (LIPSS). Although these periodic undulations have been observed since the mid-1960s [6], they have garnered increasing interest since the emergence of ultrashort lasers [7]. The characteristics of LIPSS, such as their period and orientation, depend on factors such as pulse width [8], laser fluence (pulse energy), laser polarization direction [9], laser wavelength [10, 11], the number of laser pulses [12], and the type of material being used [13]. LIPSS can be fabricated on various types of solid surfaces, including metals [14, 15, 16], semiconductors [10, 13, 17, 18], and polymers [19, 20, 21, 22].

Ultrafast lasers enable the achievement of periodicities well below the laser wavelength, spanning from a few tens of nanometers to a few microns [23, 24]. This capability encompasses metals, semiconductors, polymers, and even materials with a band-gap higher than the laser wavelength. These structures can reach amplitudes of several hundreds of nanometers, a consequence of competing ultrafast transport processes during the nonequilibrium dynamics [25, 26, 27].

LIPSS introduce distinctive functionalities to material surfaces, garnering attention across a range of applications such as surface coloring [28, 29, 30, 31], tribology for friction reduction [32, 33, 34, 35], creation of antireflection surfaces [36, 37], manipulation of surface wettability [14, 38, 39, 40], antibacterial adhesion properties [41], and enhancement of surface-enhanced Raman spectroscopy sensing [42]. For 1D structures, the key challenges revolve around achieving precise control over both amplitude and periodicity. This level of control is intricately tied to customizing laser parameters to match the characteristics of the material being irradiated. 2D structures offer an additional dimension to quadratically increase the concentration of a pattern, and crossed LIPSS, combining scales, have been the subject of recent investigations [43, 44, 45, 46].

Contemporary theories regarding the genesis of aligned LIPSS can be classified into two primary categories: electromagnetic models and self-organizational models [47, 48, 49, 50]. This dichotomy, however, is not exclusive, as it is now widely acknowledged that the observed structures are outcomes of synergistic electromagnetic and hydrodynamic influences [51, 52, 53, 54]. Models postulating the existence of electromagnetic modes delineate the energy distribution across the surface, incorporating resonances such as surface plasmon polariton, cylindrical surface waves, and surface lattice resonance [55, 56, 57]. To evoke topographic growth with symmetries linked to laser field polarization, surface-generated fields must transcend mere propagative nature. The anticipation of stationary wave generation arises from interference between incident/diffracted waves and those scattered on the microscopic rough surface, thereby intricately modulating absorbed optical energy. This paradigm is particularly salient in the formation of Low-Spatial Frequency LIPSS (LSFL) structures, where multiple indices of resonance mode hybridization become conceivable during the emergence and growth of structures amid localized ablative effects and capillary flows. For nanometric structures of the High-Spatial Frequency LIPSS (HSFL), predominantly observed during interactions with ultrafast laser beams, theories remain open due to varied ob-

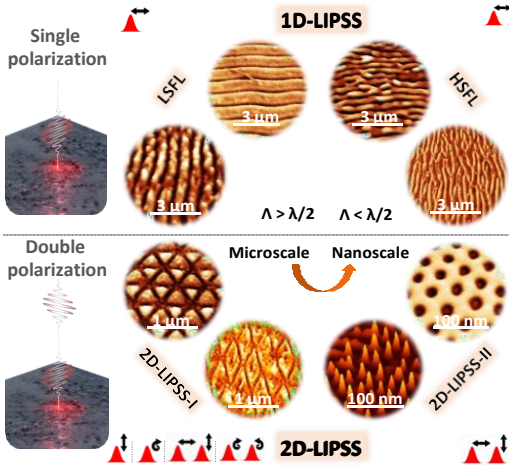


**FIGURE 1** Classification of LIPSS into distinct categories based on spatial period and scale. These categories include Low-Spatial Frequency LIPSS (LSFL), characterized by larger spatial periods, High-Spatial Frequency LIPSS (HSFL), featuring smaller periodicities, and the more intricate Two-Dimensional LIPSS (2D-LIPSS) on both the micrometric (referred as 2D-LIPSS-I) and nanometric (referred as 2D-LIPSS-II) scales. 1D-LIPSS (One-Dimensional Laser-Induced Periodic Surface Structures) primarily employs a single polarization approach, while 2D-LIPSS are mainly generated using a double polarization strategy involving crossed or circular polarizations. This strategic use of double polarization leads to an isotropic response of the irradiated surface, enabling the formation of multifaceted structures.

servations stemming from intricate dynamics [58]. The initiation of these structures seems rooted in the non-isotropic orientation of non-radiative fields around transiently created nanoreliefs. Near-field absorption induces temperature gradients, thereby instigating hydrodynamic effects such as the stretching of the liquid phase, the formation of cavitation zones, and liquid material flow attributed to the Marangoni effect [59, 60]. Recent investigations have spotlighted thermoconvective effects correlated with the genesis of these structures [61, 49, 52]. Coined as the matter reorganization theory, these concepts align with the principles of material self-organization, particularly when hydrodynamic instabilities of the Rayleigh-Bénard, Rayleigh-Marangoni, or

Rayleigh-Taylor types are implicated. Historically, self-organizational models were envisaged based on the cumulative creation of defects or surface instabilities induced by atomic diffusion and surface erosion effects [62, 63]. This perspective draws parallels to concepts proposed for modeling the effects engendered by ion beams on surfaces [64, 65, 66]. Notably, the development of models for spatially extended systems representing dissipative structures emergence proves particularly relevant, especially within the context of 2D-LIPSS.

Various types of 2D surface patterning have been reported, including patterns with hexagonal [67, 68, 69], triangular [70, 71], spherical [72], square [73], labyrinthine [74], or chaotic [75] symmetries, featuring both positive and negative reliefs such as humps [76], bumps [75], peaks [74], and spikes [77]. Achieving a remarkably uniform establishment of these microscale patterns, independently of the oriented near-field optical effects on the local nanotopography, requires a more global and collective perspective.

This review endeavors to conduct an in-depth exploration of 2D-Laser-Induced Periodic Surface Structures (2D-LIPSS) as an extension of the LIPSS phenomenon. As depicted in Figure 1, the classification of 1D-LIPSS are generally split into two categories based on their spatial period relative to the laser wavelength ( $\lambda$ ): Low-spatial frequency LIPSS (LSFL) with  $\lambda > \lambda/2$ , and high-spatial frequency LIPSS (HSFL) with  $\lambda < \lambda/2$  [13, 78]. The period and orientation of these structures, governed by the optical response - and hence the transient electronic structure - of the photoexcited material, further refine the LSFL classification. In materials exhibiting strong absorption, such as metals and semiconductors, the predominant observation entails LSFL structures with a period  $\Lambda \approx \lambda$  and an orientation perpendicular to the beam polarization. However, materials with wide bandgaps, like fused silica, display LSFL structures parallel to the beam's polarization direction. These structures exhibit periods correlated with the wavelength inside the bulk, given by  $\Lambda \approx \lambda/n$ , where  $n$  denotes the refractive index of the dielectric material [79]. In contrast, HSFL present a unique array of structures characterized by periodicities and sizes that fall well below

the optical diffraction limit. The formation of these patterns is predominantly observed under ultrashort pulse durations ranging from fs to ps. They are initiated by non-radiative optical waves, resulting in short gradient scale lengths and periodicity. Importantly, this periodicity does not stem from interference patterns, but rather emerges as a consequence of hydrodynamic convection instability within a thin melted layer that is disrupted by the excited pressure wave [54].

In this manuscript, the transition from the LIPSS to 2D-LIPSS formation is presented. Furthermore, the review originally compiles observations of 2D structures at various scales and aims to categorize the different 2D-LIPSS configurations investigated by various research groups, classifying them based on their periodicity. Throughout this examination, the emphasis is placed on the intricate process of generating 2D-LIPSS-II structures at the finest scale. The analysis delves into a thorough discussion of critical parameters influencing symmetry creation, including aspects such as polarization, feedback concentration, and aspect ratio control. Additionally, we establish that the interplay between convective flows and polarization-dependent photoexcitation serves as a primary mechanism for manipulating the symmetries of 2D patterns. This intricate instability mechanism is reinforced by thorough experimental observations and validation. This review concludes by addressing its limitations and suggesting potential research directions in the domain of nanotexturation prediction.

## 2 | FROM LIPSS TO 2D-LIPSS

Beam engineering is the key for transforming general LIPSS to 2D-LIPSS. In this section, the different parts of LIPSS with respect to laser parameters are presented, highlighting how temporal beam engineering transforms LIPSS into 2D-LIPSS-II through precise time delay control.

Historically, LIPSS have been produced on different surfaces using coherent light sources with a single polarization. As depicted in Figure 2, a comparison between

the 1D and 2D morphological maps showcases characteristic surface formations on steel surfaces after ultrafast laser irradiation at various parameters. In Figure 2 (A), the morphological map of LIPSS illustrates that the number of pulses and the peak fluence of the laser are the two pivotal factors governing these LIPSS variations. For instance, progressively augmenting the fluence and number of pulses allows for the transformation of the initial surface topography into high-spatial frequency LIPSS (HSFL), low-spatial frequency LIPSS (LSFL) [88], grooves [89], and spikes [90]. These structures can be readily produced through single polarization. However, 2D-LIPSS have been mainly generated by a dual-pulse laser setup incorporating a Mach-Zehnder interferometer. As a result, time-delay emerges as a supplementary crucial parameter influencing the formation of the recently observed 2D-LIPSS-I and II structures, as depicted in Figure 2 (B) and (C).

In Figure 2 (D), an experimental setup for 2D-LIPSS is illustrated. In brief, for general LIPSS, a single polarization is sufficient, and these can be generated through either static or multiple pulses on large surfaces via an optical galvano scanner. To disrupt surface isotropy and transition from LIPSS to 2D-LIPSS, dual polarization plays an important role in fine-tuning nanostructures within a controllable regime. However, it is not mandatory to obtain 2D-LIPSS-I. The use of a galvano scanner is required for 2D-LIPSS-I, which is distinct from 2D-LIPSS-II, reported through both methods. Moreover, Figure 2 (A) presents the positioning of 2D-LIPSS-II with respect to general LIPSS in terms of laser dose. Clearly, parameters in proximity to LSFL and HSFL formation allow the transformation of a 1D surface on the scale of hundreds of nanometers to a 2D-LIPSS-II surface on the scale of tens of nanometers. This transition is accomplished through the use of a double pulse with carefully controlled time delay.

Tables 1 and 2 provide a clear literature review of 2D-LIPSS-I and 2D-LIPSS-II formation, respectively, on various common metals induced by fs-laser pulse irradiation. The entries are categorized based on pattern size and periodicity, offering an insightful overview of the field. Remarkably, 2D-LIPSS-I can manifest across a

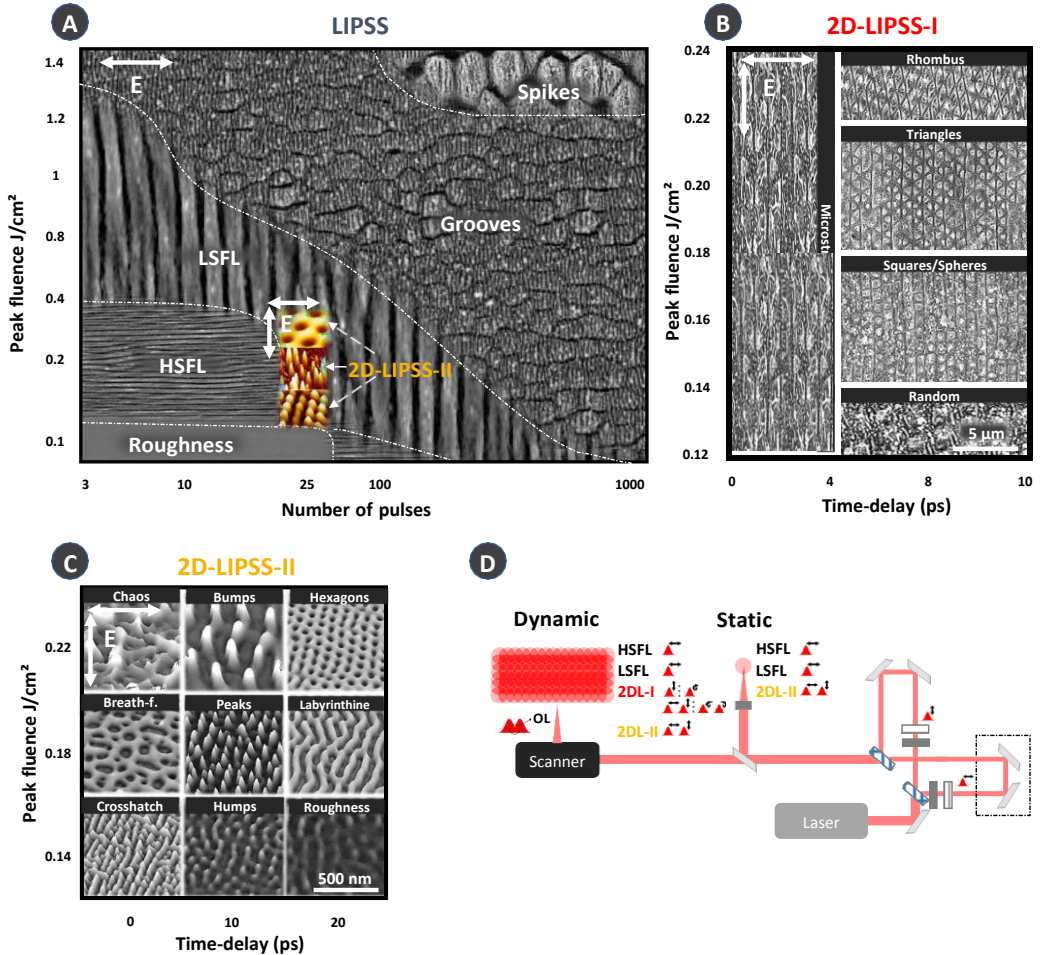


**FIGURE 2** A: Morphological map illustrating distinct surface morphologies (HSFL, LSFL, grooves, and spikes) developed on steel surfaces through ultrafast laser irradiation, with adjustments to irradiation parameters. Reproduced with permission [80]. Copyright 2018, MDPI publisher. B: Morphological map of 2D-LIPSS-I surface with different laser fluences and time delays, under irradiation of two temporally delayed femtosecond laser beams on cobalt. Reproduced with permission [72]. Copyright 2019, IOP publisher. C: Morphological map of 2D-LIPSS-II as a function of the peak fluence and time-delay imposed between the pulses of a double pulse sequence with a Number of double-pulse sequences  $N = 25$ . Reproduced with permission [75]. Copyright 2022, The Authors, Springer Science publisher. D: Experimental setup for 2D-LIPSS, using Mach-Zhender interferometer, with static irradiation for 2D-LIPSS-II and coupled with Galvo scanner for 2D-LIPSS-I and II.

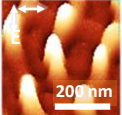
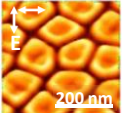
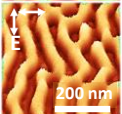
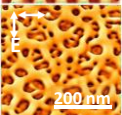
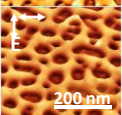
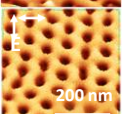
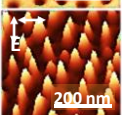
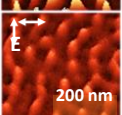
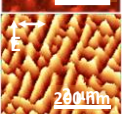
spectrum of pattern symmetries, including patterns with hexagonal [67, 68, 69], triangular [70, 71, 83], square [72, 73], rhombus [85] and conical [81, 91], on diverse materials like cobalt, titanium, stainless steel, tungsten

and others. Moreover, the scope of their size range is quite extensive, spanning from several microns down to the hundreds of nanometers.

Conversely, the dimensions of 2D-LIPSS-II are no-

$\Lambda$ (nm)	$\Omega$ (nm)	Materials	2D-LIPSS-I	References	Patterns
15000	10000	Si	Hexagons	Reproduced from [67]	
1000	400	W	Microcones	Reproduced from [81]	
900	700	CoCrMo	Triangles	Reproduced from [82]	
800	500	X6Cr17	Triangles	Reproduced from [83]	
700	600	Co	Rhombus	Reproduced from [72]	
700	500	St(316L)	Squares	Reproduced from [84]	
700	400	Ti	Triangles	Reproduced from [71]	
700	400	Co	Triangles	Reproduced from [72]	
600	300	St(316L)	Triangles	Reproduced from [85]	
400	300	Si	Hexagonal cavities	Reproduced from [68]	
355	100	Ni5W tape	Hexagonal protrusions	Reproduced from [86]	

**TABLE 1** Literature survey of 2D-LIPSS-I reported on diverse materials upon fs-laser pulse irradiation. Here,  $\Lambda$  represents the pattern periodicity, and  $\Omega$  corresponds to the pattern width. The images are presented in pseudo-3D scanning electron microscopy. The polarization of the laser pulses is indicated by white arrows.

$\Lambda$ (nm)	$\Omega$ (nm)	H (nm)	Materials	2D-LIPSS-II	References	Patterns
150	65	110	Ni	Nanobumps	Reproduced from [76]	
120	100	100	C	Nanobumps	Reproduced from [87]	
100	50	30	Ni	Nanolabyrinthine	Reproduced from [77]	
80	40	20	Ti	Nanobreathtaking	Reproduced from [74]	
80	40	20	Ni	Nanobreathtaking	Reproduced from [75]	
80	30	20	Ni	Nanohexagons	Reproduced from [69]	
70	20	100	Ni	Nanopeaks	Reproduced from [77]	
50	30	15	Ni	Nanohumps	Reproduced from [76]	
40	30	20	Ni	Nanocrosshatch	Reproduced from [77]	

**TABLE 2** Literature survey of 2D-LIPSS-II reported on diverse materials upon fs-laser pulse irradiation. Here,  $\Lambda$  represents the pattern periodicity,  $\Omega$  denotes the pattern width, and H corresponds to the height. The images are presented in pseudo-3D scanning electron microscopy. The polarization of the laser pulses is indicated by white arrows.

tably smaller as presented in Table 2, varying from 10 to 500 times less in size, encompassing a range from 150 nanometers down to 20 nanometers. These meticulously arranged structures are reported across diverse materials, including diamond, titanium and

nickel. These structures exhibit an array of shapes, such as nanohexagons [69], nanobumps [76, 87], nanohumps [76], nanocrosshatch [77], nanobreathtaking [74], nanolabyrinthine patterns [77], and high aspect ratio nanopeaks [92].

In general, HSFL are created by thermal convection, which arises from the interplay of light absorption fluctuations caused by surface reliefs and the fluid dynamics of the free surface between laser pulses. These optical absorption fluctuations create localized regions of inhomogeneous energy confinement within the material. The amplification mechanism in thermoconvection involves a positive feedback loop in which temperature gradients, convective flow, and pressure forces interact to generate well-defined flow patterns.

In the context of 2D-LIPSS, understanding the nonlinear mechanisms governing symmetry breaking and pattern selection in convective instabilities remains a complex challenge, making the transition conditions from one self-organization regime to another difficult to predict [93]. In a general sense, these nanostructures emerge during the interplay of pressure gradient forces, mainly driven by surface tension and cavitation processes (through rarefaction), along with the rapid resolidification of the molten surface region. Thermoconvective instabilities can induce fluid flow due to comparable transverse and longitudinal thermal gradients [52, 94]. The use of two orthogonal electric field polarizations significantly favors the formation of 2D symmetries. Specific laser parameters, such as peak fluence, time delay, and the number of double-pulse sequences, exert a crucial influence on thermally-driven convection characteristics, thereby impacting surface morphology and topography. Therefore, irradiation conditions play a pivotal role in determining the emergence, growth, and control of pattern development. Further mechanisms for 2D-LIPSS-II will be discussed in Section 5 of this review.

The following sections provides an in-depth exploration of its respective 2D-LIPSS category, alongside a comparative analysis involving relevant research in the field. The distinguishing characteristics that set 2D-LIPSS I apart and their societal implications are elucidated. Additionally, the discussion encompasses a comprehensive overview of research related to 2D-LIPSS-II, accompanied by a detailed explanation of the mechanisms driving their formation.

### 3 | 2D-LIPSS AT THE LASER WAVELENGTH SCALE

In 1999, Kawakami et al. uncovered a significant finding in self-assembled structures by identifying emergence of microcones arrays on crystalline tungsten [81, 91]. The Atomic Force Microscopy (AFM) examination of the tungsten surface irradiated with nanosecond laser pulses revealed two distinct scenarios.

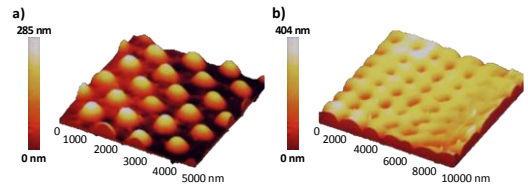


**FIGURE 3** Atomic Force Microscopy (AFM) trace of the laser-irradiated tungsten surface. (a) Irradiated at an angle of incidence  $\theta = 4^\circ$  with a p-polarized beam, revealing the presence of microcones structures arranged in a hexagonal pattern with an array spacing of approximately  $1 \mu\text{m}$ . The height of these structures measures about  $300 \text{ nm}$ . (b) Irradiated at an angle of incidence  $\theta = 23^\circ$  with an s-polarized beam, capturing an intermediate stage in the coherent array formation process. The spacing between these arrays measures about  $1.5 \mu\text{m}$ . Adapted with permission [81]. Copyright 1999, Elsevier publisher

Firstly, at an incidence angle  $\theta = 4^\circ$  with a p-polarized beam, the resulting AFM trace unveiled the intriguing presence of ultrafine particles, known as microcones, meticulously organized in a hexagonal configuration, as presented in Figure 3 (a). The inter-microcones spacing forms a pattern with an average distance of about  $1 \mu\text{m}$ , with an elevation of approximately  $300 \text{ nm}$ . Intriguingly, these microcones displayed a hexagonal or square arrangement, a phenomenon that challenges the conventional explanation provided by the LIPSS formation theory, even for circularly polarized pulses. The authors successfully produced tungsten microcones with an aspect ratio exceeding 6 through laser irradiation in an inert gas atmosphere. Notably, they refined the structural characteristics by reducing the radius of curvature



to less than 100 nm through chemical etching of the initially formed microcones, which had a larger radius of curvature. [95].

Secondly, under an angle of incidence  $\theta = 23^\circ$  with an s-polarized beam, the AFM analysis captures an intermediate stage within the coherent array formation process, recently identified as hexagons, as presented in Figure 3 (b). The observed arrays exhibit a larger spacing, measuring around 1.5  $\mu\text{m}$ . This comprehensive examination provided valuable insights into the surface morphology alterations induced by laser irradiation at varying incident angles and polarization states at that time.

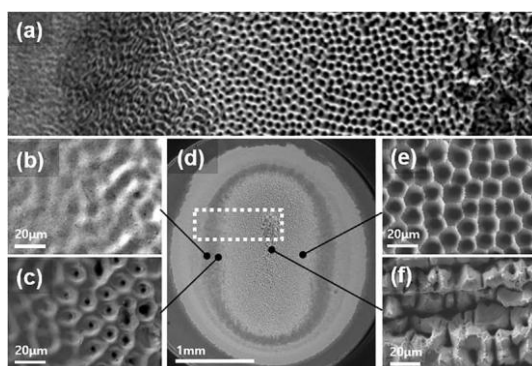


**FIGURE 4** Scanning Electron Microscope (SEM) images of a silicon surface irradiated by 72000 - 532 nm nanosecond ( $< 10$  ns) laser pulses in a water medium, (a) Magnified image of the dashed rectangular area in (d) revealing a honeycomb of hexagonal structures, (b) capillary wave formation in outer areas, (c) convection cells (Concaves and holes) in the boundary area, (d) full image of the beam spot on the silicon surface, (e) porous structure in the inner area, (f) breakdown of the wall of the unit cell in the center. Reproduced with permission [67]. Copyright 2019, Elsevier publisher.

Moreover, in 2019, J.G. Son et al. observed the formation of a self-organized microporous concave cell array, a subtype of 2D-LIPSS-I, on a large scale [67]. They achieved this by using pulsed nanosecond laser interactions with silicon in an aqueous medium. The resulting periodicity of these structures ranged between 10 and 15  $\mu\text{m}$ , as presented in Figure 4. In this case, the rapid generation of a thermal gradient by the laser induces

shear strain and initiates deformations in the molecular-scale lattice structure. These initial lattice defects establish a critical foundation for subsequent shape alterations.

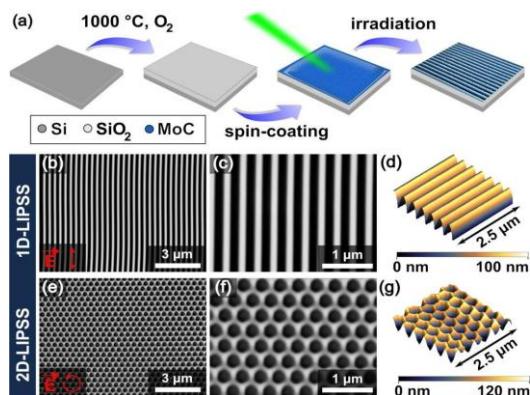


**FIGURE 5** Sample preparation and subwavelength surface patterning of metal-organic thin films ( $[\text{Mo}_2\text{S}_4(\text{S}_2\text{CN}^n \text{Bu}_2)_2]$  (MoC)) with 1D and 2D structures. (a) Sample preparation scheme. (b, c, e, f) Electron microscopic images of 1D (b, c) and 2D-LIPSS-I (e, f), which were generated by irradiating a spin-coated MoC thin film with linear or circularly polarized light. (d, g) AFM images of 1D (d) and 2D-LIPSS-I (g). Reproduced with permission [68]. Copyright 2022, American Chemical Society publisher.

2D-LIPSS-I were also reported in the work of Durbach et al., who investigated thin films crafted from a metal-organic precursor of  $\text{MoS}_2$  as shown in Figure 5. They achieved the formation of periodic structures by controlling the laser wavelength, MoC film thickness, and substrate characteristics, all while varying the thicknesses of  $\text{SiO}_2$  layers [68]. The resulting organized nanostructures shown in Figure 5 exhibited a periodicity of 300 nm and a depth of 100 nm.

In 2018, Romano et al. identified a distinct category of nanostructures on stainless steel ranging in scale from hundreds of nanometers to the laser wavelength, termed 2D-LIPSS-I in this review [83]. These structures exhibit triangular shapes and were produced using a femtosecond laser with a wavelength of 1032 nm, a pulse duration of 310 fs, and singular circular polariza-

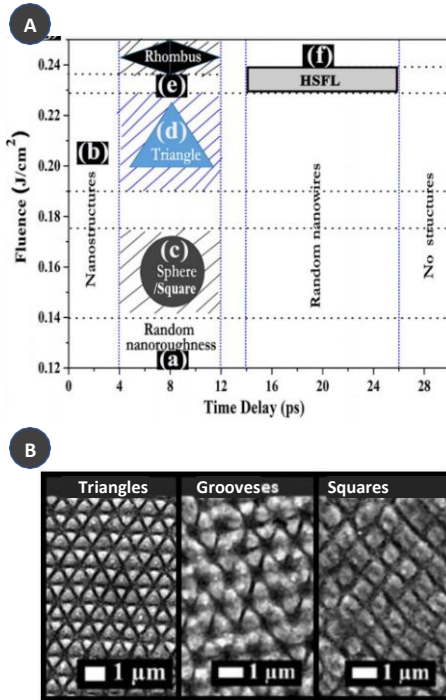


**FIGURE 6** A: Parameter space for 2D surface structures on cobalt with different laser fluences and time delays, under irradiation of two temporally delayed femtosecond laser beams. (a) Random roughness, (b) Extensive structures, (c) Spherical or square structures, (d) Triangular structures and (e) rhombic structures. . . Reproduced with permission [72]. Copyright 2019, American Institute of Physics publisher. B: SEM images of stainless steel surface irradiated with different laser parameters. Reproduced with permission [84]. Copyright 2019, Elsevier publisher.

tion integrated with a Galvo scanner. One year later, Fragelakis et al. extended these findings to the development of similar nanostructures on the same material. They employed a Mach-Zehnder interferometer in conjunction with two circular or crossed linear polarizations, providing additional fine-tuning control over these nanostructures [84]. Figure 6 (A) provides a visual representation, demonstrating the influential roles that both time delay and laser fluence exert in governing the 2D surface morphology of these structures [72]. Figure 6 (B) showcases the observation of triangular struc-

tures facilitated by the employment of two circular and crossed polarizations, with time delays of 5 ps. Conversely, grooves and squares nanostructures manifested at time delays of 0.5 ns. The explanation was attributed to the microfluidic movement of molten material following irradiation [96]. Convection flow patterns are expected to appear in the temporarily formed liquid experiencing inhomogeneous and pronounced temperature gradients. In certain scenarios, diverse convection flow patterns cyclically alternate following the imposition of a temperature gradient [97]. Hydrodynamic simulations associate the formation of grooves and spikes in silicon as well as grooves in fused silica, with Marangoni convective roll flow [49, 94]. This specific form of convection flow is driven by temperature gradients along the material's surface, underscoring the significance of the balance between kinematic viscosity and thermal diffusivity, as characterized by the Prandtl number [49, 84]. Furthermore, various groups have embarked on the exploration of diverse categories of 2D-LIPSS-I on alternative materials, driven by the notable industrial potential attributed to these structures. In particular, Jalil et al. unveiled the emergence of rhombus, triangular, and spherical or square structures on cobalt [72] employing similar double pulse irradiation sequences, outlined in Figure 2 (B).

## 4 | 2D-LIPSS AT THE NANOSCALE

Driven by near-field light enhancement, periodic patterns have approached ultimate scales down to tens of nanometers. This advancement was demonstrated by Abou Saleh et al. in 2020 [69]. Using single crystal metallic samples, a self-organized pattern of distinct nanohexagons, each measuring 20 nanometers in diameter and exhibiting a periodicity as small as 60 nanometers, was induced on a Nickel surface oriented along the (001) plane. This was achieved by overcoming the anisotropic polarization response of the surface through a delayed action of cross-polarized laser pulses. This groundbreaking development, alleviating the directional effects compelled by a linear laser polarization, paved

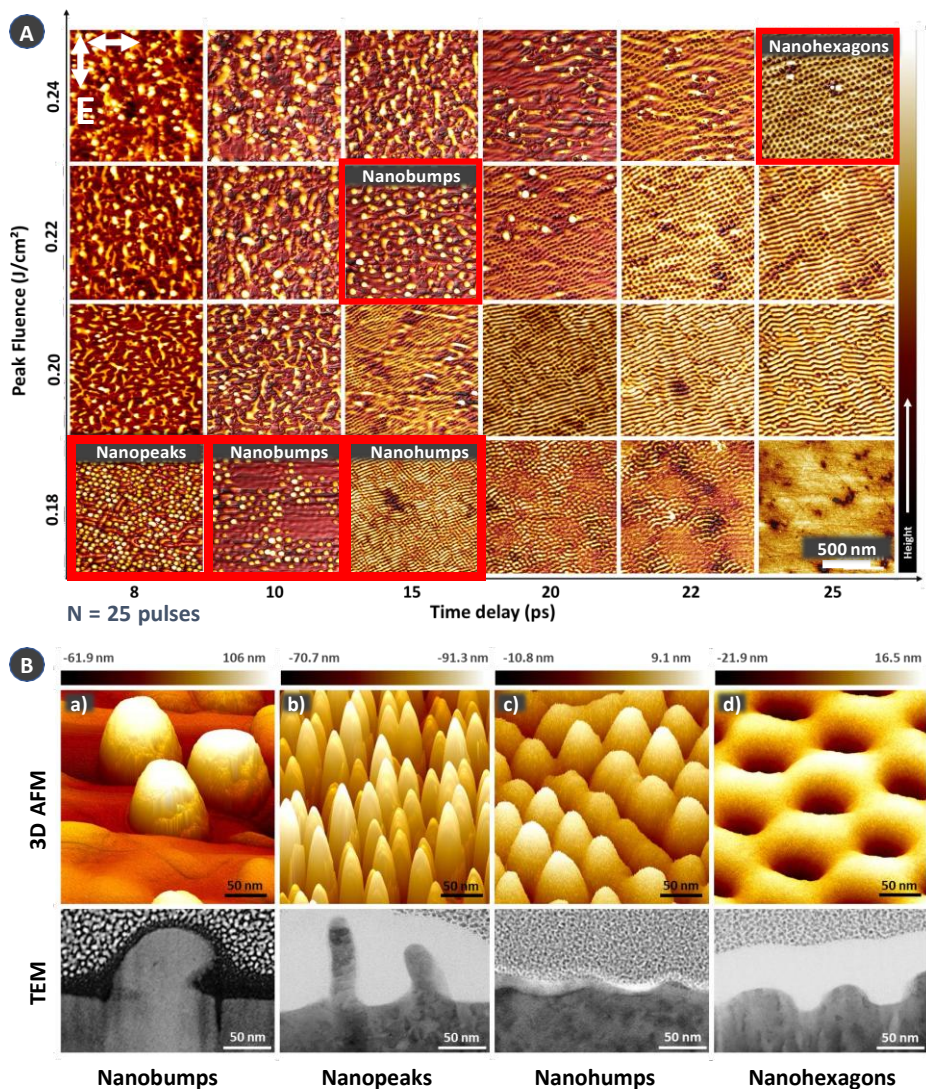


**FIGURE 7** A: 2D AFM morphological map of laser-induced nanopatterns formation on Ni(001) as a function of time delay and peak fluence at a fixed number of double-pulse sequences ( $N_{DP S}$ ) of 25. The different zones of interest are nanopeaks, nanobumps, nanohumps and nanohexagons. They are created progressively at different doses: (0.18  $J/cm^2$ ; 8 ps), (0.18  $J/cm^2$ ; 10 ps), (0.18  $J/cm^2$ ; 15 ps), (0.24  $J/cm^2$ ; 25ps). B: 3D AFM of the nanobumps (a), nanopeaks (b), nanohumps (c) and nanohexagons (d) presenting the nanostructures height and distribution. Transmission electron microscopy of the principles nanostructures presenting the cross sectional view of nanostructures. The polarization of the laser pulses is indicated by white arrows. Reproduced with permission [75, 76]. Copyright 2022, The Authors, Springer Science publisher. Copyright 2021, The Authors, MDPI publisher.

the way for autonomous topographical assembly at the nanoscale.

More recently, Nakhoul et al. delved into an array of nanopatterns, each corresponding to distinct self-organization regimes driven by convection mechanisms at the nanoscale, through their investigation of femtosecond laser-irradiated nickel surfaces [75, 76, 77]. Figure 7 (A) portrays original 2D AFM images illustrating the formation of laser-induced nanopatterns, masterminded by the manipulation of both the laser peak fluence (ranging from  $0.18 \text{ J/cm}^2$  to  $0.24 \text{ J/cm}^2$ ) and the time delay ( $\Delta t$ , varying from 8 ps to 25 ps). Notably, at low  $\Delta t$  values (8 ps and 10 ps) and peak fluences above  $0.20 \text{ J/cm}^2$ , the observation of chaotic nanostructures emerged. This chaotic behavior is also witnessed at (15 ps ;  $0.24 \text{ J/cm}^2$ ), particularly when employing a tight time-delay interval between pulses. Energetically, this mechanism mimics a single-pulse sequences process with  $N=25$ , where the cumulative absorbed fluence exceeds the absorbed threshold of a single-pulse sequences due to the marginal delay, which triggers a minor reduction in Ni reflectivity caused by electronic thermal excitation before the arrival of the second pulse [98].

At  $0.18 \text{ J/cm}^2$ , three distinct nanopattern types emerged at 8 ps, 10 ps, and 15 ps. Notably, the tallest nanostructures surfaced at  $\Delta t = 8$  ps, sporting a configuration akin to a karst peak, aptly dubbed "nanopeaks". With larger time delays of 10 ps, the shape of these nanostructures transformed, exhibiting an augmented diameter resembling "nanobumps". At  $\Delta t = 15$  ps, the height of the nanostructures markedly diminished, leading to their classification as "nanohumps". Notably, a gradual disappearance of these nanostructures occurred as the time delay increased from 15 ps to 25 ps. During this interval, the cumulative energy dissipated, and the polarization memory was erased through thermal dissipation preceding the arrival of the second pulse.

At  $0.20$  and  $0.22 \text{ J/cm}^2$ , the transition from chaotic structures to stripes can be observed, passing through a transition regime at ( $0.20 \text{ J/cm}^2$ ; 15 ps and  $0.22 \text{ J/cm}^2$ ; 20 ps). This transition region has a short range order, which consists of locally nanobumps and chaotic nanos-

tructures. However, at  $\Delta t = 25$  ps, labyrinthine patterns surfaced, a phenomenon documented previously as disordered spatial structures exhibiting a truncated short-range order [99]. At  $0.24 \text{ J/cm}^2$ , the transition from disordered nanostructures to a nanocavity pattern transpired as  $\Delta t$  increased, traversing a transitional domain from 15 to 20 ps. The hexagonal array of nanocavities was previously noted under analogous parameters [69].

Figure 7 (B) showcases 3D images captured by atomic force microscopy (AFM) and transmission electron microscopy (TEM) of the principal nanostructures introduced earlier. In the AFM images, the notable height of the nanobumps is evident, reaching approximately 100 nanometers, with the cross-sectional view highlighting a similar diameter of  $\sim 100$  nanometers. A highest aspect ratio is obtained for nanopeaks that exhibit an approximate height of 100 nanometers and a diameter of about 20 nanometers. Conversely, the nanohumps exhibit a more modest height, approximately 10 nanometers, within the context of these organized nanostructures, paired with a diameter of roughly 25 nanometers. Furthermore, the nanocavity nanostructures exhibit a hexagonal arrangement, presenting a depth of roughly 20 nanometers and a diameter of about 30 nanometers, as delineated in the cross-sectional image. Worth noting is the absence of any discernible ablation craters, evident in both the AFM and TEM observations, even in scenarios involving the highest pulse counts. Remarkably, this confirms the preservation of a regime characterized by the formation of a liquid layer, precluding ablation process. Thus, the system consistently resides within the regime of melting and swelling.

In a recent development, an additional variety of 2D-LIPSS-II has come to light on diamond surfaces, unveiled by Matteo et al. in 2021 [87]. The authors harnessed a Michelson-like interferometer to generate time-delayed cross-polarized double pulses, as illustrated in Figure 8. It was observed the formation of 80 nm 2D-LIPSS on single-crystal and polycrystalline diamond surfaces. The periodicity of these nanostructures can be controlled in the range  $\lambda/4 \geq \Lambda \geq \lambda/10$ . These 2D laser-induced periodic surface structure exhibited remarkable

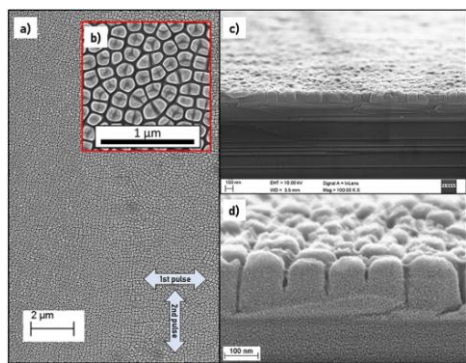


**FIGURE 8** Top view (a, b) of the nanotextures obtained at  $F = 2.16 \text{ J/cm}^2$ ,  $\Delta t = 500 \text{ fs}$ , scanning speed of  $0.75 \text{ mm/s}$ . Cross-section view at different magnifications (c,d). The arrows indicate the polarization directions. Reproduced with permission [87]. Copyright 2021, American Chemical Society publisher.

anti-reflection properties after removing surface debris by chemical etching, which increased the absorption rate of visible light by 50 times.

#### 4.1 | Patterns in symmetry breaking transition

Figure 9 (A) illustrates a spectrum of organizational patterns governed by the laser fluence and the time delay between two cross-polarized pulses. These patterns emerge within a framework of a constant number of 25 double-pulse sequences and a pulse duration of approximately 100 femtoseconds. Notably, a total of eight distinct organizational modes were observed.

Within the chaotic regime, realized at low  $\Delta t$  values ( $\leq 14 \text{ ps}$ ) and laser fluences ranging between  $0.19$  and  $0.24 \text{ J/cm}^2$ , the system exhibited a disordered arrangement. Nanobreath-figure patterns were observed in a more constrained region characterized by  $\Delta t \approx 0 \text{ ps}$ , specifically within the range of laser fluences spanning from  $0.20$  to  $0.22 \text{ J/cm}^2$ . These nanopatterns assumed the form of unorganized cavity structures, featuring nanoscale dimensions [100][101]. Furthermore, the manifestation of nanocrosshatch patterns occurred at  $\Delta t \approx 0 \text{ ps}$ , yet this time at lower laser fluences, within

the range of  $0.17$  to  $0.19 \text{ J/cm}^2$ . In this configuration, the patterns consisted of two diagonal nanostripes perpendicularly superimposed upon each other.

As the time delay spans the range from  $6 \text{ ps}$  to  $10 \text{ ps}$ , the transformation of nanocrosshatch patterns unfolds into the emergence of high aspect ratio nanopeaks. These nanopeaks, characterized by a diameter of approximately  $20 \text{ nm}$  and a towering height of about  $100 \text{ nm}$  [77], come into being. By extending the time delay further, the energy feedthrough significantly influences the flow dynamics, leading to a transition in the nanopeak pattern towards a new configuration. Although the height remains comparable to that of the original nanopeaks, their diameter expands to approximately  $100 \text{ nm}$ , resulting in a reduced concentration. Consequently, the nanopeak regime transforms into a nanobumps regime, characterized by a relatively diminished aspect ratio.

The onset of nanohumps regime materializes when the time delay attains values greater than or equal to  $10 \text{ ps}$ . These structures manifest as small humps, characterized by a modest aspect ratio and a height of roughly  $10 \text{ nm}$ . Meanwhile, the emergence of nanovoids or nanohexagons is evident at higher energy levels, exceeding  $0.19 \text{ J/cm}^2$ . Notably, their size escalates with the augmentation of the laser fluence, ultimately culminating in homogeneous shapes and arrangements observed at a laser fluence of  $0.24 \text{ J/cm}^2$  and a time delay of  $24 \text{ ps}$ .

Furthermore, a distinct class of labyrinthine nanostructures is observable within a realm of high laser fluences, falling between  $0.22$  and  $0.24 \text{ J/cm}^2$ . This intricate labyrinthine configuration takes form over a wide time-delay range, spanning from  $28 \text{ ps}$  to  $30 \text{ ps}$ . The enthralling labyrinthine shape materializes precisely at a laser fluence of  $0.23 \text{ J/cm}^2$  and a time delay of  $30 \text{ ps}$ .

As presented previously, the different 2D-LIPSS patterns are obtained reproducibly by controlling several influential parameters. In particular, a cross-polarization strategy is deftly employed to foster isotropic energy deposition, thereby facilitating the process of self-organization. The polarization state of the incident pulses in the double-pulse sequence has a major influ-

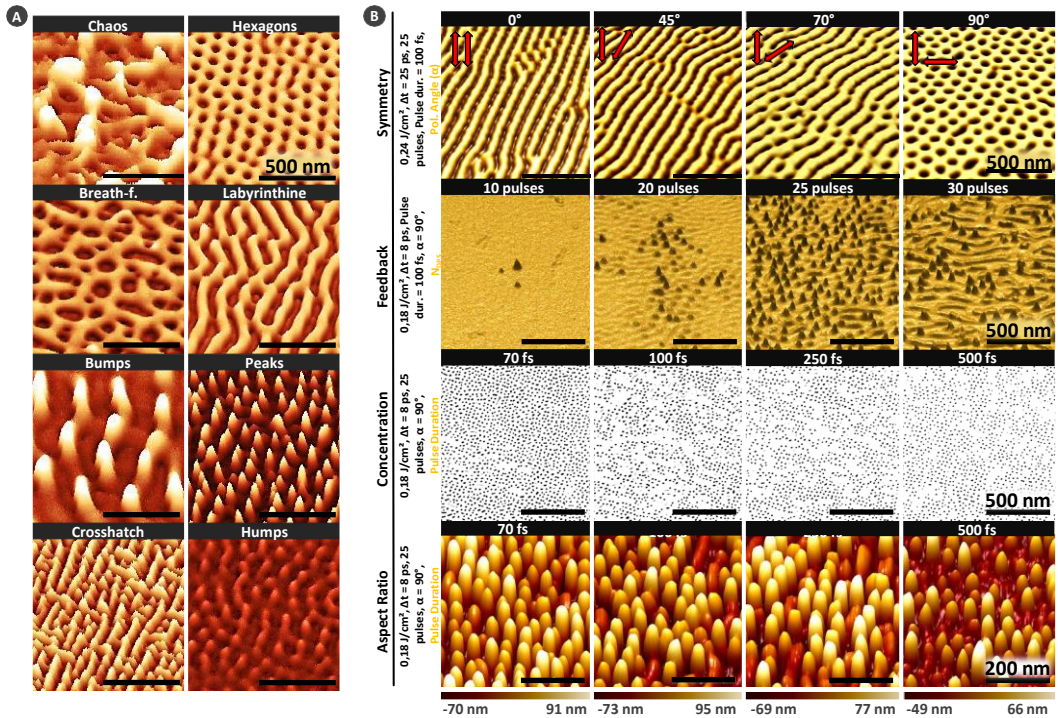


**FIGURE 9** A: Pseudo-3D SEM of nanostructures in different pattern regimes as chaos, nanobreathe-figure, nanocrosshatch, nanobumps, nanopеaks, nanohumps, nanohexagons and nanolabyrinthine. B: Impact of the polarization angle between the first and second pulse in inducing an isotropic response, the pivotal role of feedback and the number of pulses in the formation of nanostructures (for the nanopеaks case), and the influence of pulse duration in regulating nanostructure concentration and aspect ratio. The fixed laser parameters are presented in black, and the variable parameters in orange. The material used in the figure is Ni(001). Reproduced with permission[76, 77]. Copyright 2021, The Authors, MDPI publisher. Copyright 2022, The Authors, Wiley publisher.

ence on the nanostructures created, as presented in Figure 9 (B). The polarization angle itself is meticulously controlled through the integration of a half-wave plate within the Mach-Zehnder interferometer's optical pathways. In instances where two pulses impact the surface with identical polarization orientations ( $\alpha = 0^\circ$ ), nanoripples with periodicities closely approximating 60 nanometers emerge, arrayed in parallel alignment with the incident polarization, as illustrated in Figure 9 (B). However, when the polarization of the second pulse is rotated by a half-wave plate ( $0^\circ \leq \alpha \leq 45^\circ$ ), the nanostripes pattern appears, with no preference to the polarization orientation. Notably, the morphological shape of these nanoripples evolves as the polarization angle

extends, specifically within the range of  $45^\circ < \alpha < 90^\circ$ , accompanied by a transitional regime marked by the emergence of nanohexagons amidst the nanoripple landscape. When  $\alpha$  assumes a value of  $90^\circ$ , implying the crossing of polarizations for the two-delayed pulses, the outcome is the spontaneous formation of self-organized nanohexagons across the surface.

To investigate the role of number of double-pulse sequences ( $N_{DPS}$ ) in organization and stabilization of nanopatterns, a constant laser fluence of  $0.18 \text{ J/cm}^2$  and a time delay  $\Delta t$  of 8 ps were maintained. The parameter  $N_{DPS}$  was intentionally varied across the spectrum, ranging from 0 to 50 pulses. This strategic manipulation aimed to unravel the integral role of  $N_{DPS}$  in orchestrat-

ing the self-organization of nanostructures.

To illustrate, even a slight alteration in the number of pulses can potentially yield a comprehensive transformation in both the nature and density of the resulting nanostructures. In the range of 1 pulse to 10 pulses for  $N_{DP,S}$ , no discernible nanostructures were observed. The need for a higher count of double-pulse sequences became evident, as the cumulative irradiated energy remained below the thresholds essential for surface modification or the initiation of nanostructure formation. However, the scenario changed notably when  $N_{DP,S}$  reached 20 pulses, as illustrated by the pseudo-3D image revealing the emergence of a limited number of peaks on the surface. The subsequent increase to  $N_{DP,S} = 25$  pulses led to a progressive enhancement in the organization, concentration, and height of these peaks. As the number of double-pulse sequences further ascended to 30 pulses, a diminution in peak concentration was noted, accompanied by the advent of other structural configurations. In the final stretch, spanning 38 pulses to 50 pulses for  $N_{DP,S}$ , the formerly organized nanostructures surrendered their existence, supplanted by an emergence of chaotic nanostructures. Consequently, to align with these tendencies, the ensuing investigations judiciously fixed the number of double-pulse sequences within close proximity to the organizational regimes, anchoring it around  $N_{DP,S} \approx 25$  pulses.

The pulse duration emerges as an additional factor in finely controlling surface morphology. The manipulation of nanopeak concentration, as portrayed in Figure 9 (B), underscores the pronounced impact of pulse duration. It becomes evident that reducing the pulse duration from 500 to 100 femtoseconds results in an almost twofold increase in concentration. A comparable influence can be observed for nanopeaks, where a modification in both concentration and cavity morphology becomes apparent, as the pulse duration is diminished from 250 to 150 femtoseconds. In this context, it becomes manifest that pulse duration exerts a profound influence in shaping both the form and concentration of the resultant nanostructures, rendering them amenable and adaptable to diverse applications [77, 74].

## 5 | 2D-LIPSS DRIVEN BY THERMO-CONVECTION

The evolution of structures can be contingent on the temperatures achieved within the material, encompassing parameters such as the melting temperature, evaporation temperature, as well as transport properties like kinematic viscosity and thermal diffusivity. The energy delivered to the surface propagates into the lattice, undergoing conversion into kinetic energy, and thereby potentially triggering the expulsion of materials and particles. This phenomenon is commonly referred to as laser ablation [102, 103]. In Figure 10 (a-f), the primary ablation mechanisms governing the initial stages of surface removal and nanoroughness formation in the low fluence regime are delineated, showcasing the effect of increasing irradiation fluence. Predominantly, these mechanisms involve processes like melting and resolidification, cavitation, spallation phenomena, or the decomposition of materials due to explosive boiling. A visual representation of a metallic material's region, subjected to ultrashort laser irradiation, is illustrated in Figure 10 (g), garnered from a conventional molecular dynamics simulation [24]. This figure offers insight into some of the ablation-inducing mechanisms over the course of the simulation, accompanied by indications of the scales of the affected layers and the components subjected to ablation.

Consequently, a diverse array of topographical alterations can manifest on the irradiated material's surface, stemming from the distinct mechanisms precipitating material ablation. These variations are inherently contingent on the distinctive material categories involved.

### 5.1 | Polarisation-oriented field enhancement and optical feedback

As shown in Figure 9 (B), nanopeaks were formed through a feedback process. Each pulse irradiates a surface that has already been altered by the previous pulse. This is true for all 2D-LIPSS-II observations. Figure 11 (A) shows a high-resolution AFM image of the formation of convection cells at a low number of pulses prior to

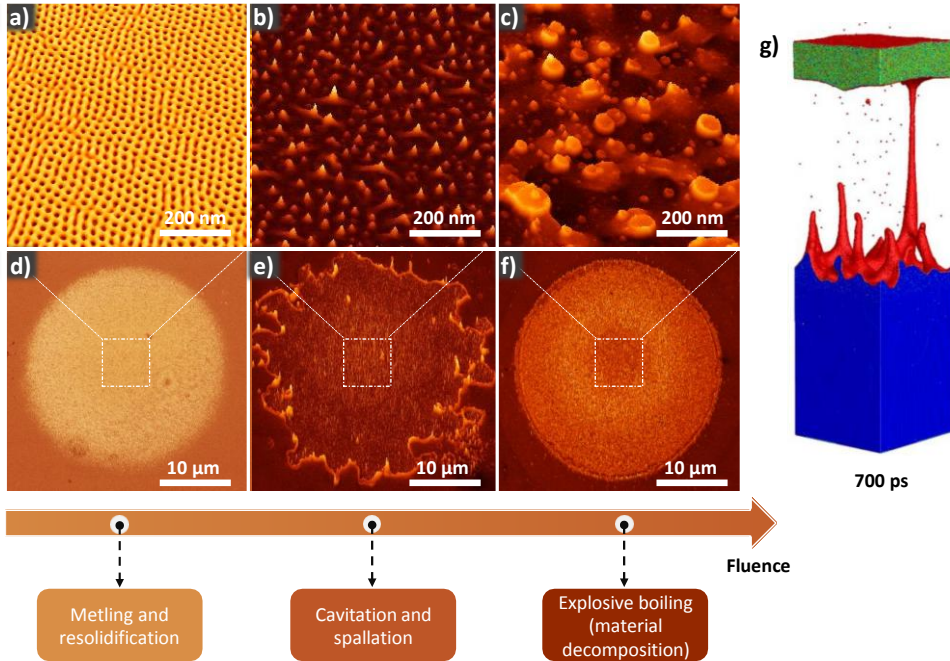


**FIGURE 10** Primary mechanisms governing surface reorganization with respect to varying fluence levels. At sub-spallation fluences, the system undergoes melting and resolidification (a, d). In the sub-phase explosion regime, cavitation of the melting region results in the ejection of a liquid layer from the target's surface (b, e, g). Beyond the phase explosion threshold, increasing fluence leads to the ejection of multiple liquid layers and material ablation (c, f). The material used in the figure is Ni(001). (g) Molecular dynamics simulation illustrating the formation of topography under ultrafast laser-induced spallation. Reproduced with permission [24]. Copyright 2018, The Authors, Springer Science publisher.

the formation of nanopeaks. The feedback process resulted in the formation of nanopeaks on the edges of these convection cells.

For coherently generated scattering fields that give rise to radiative waves inducing structures close to the wavelength (LSFL), the nature of surface imperfections leading to light scattering is inconsequential. However, when the incident field couples with surface fluctuations at the nanoscale, the type of imperfection, whether it be a protrusion or a depression, results in an enhancement of the non-radiative field oriented along the polarization [9, 78]. The polarization dependence of intensity maxima around a nanorelief, akin to a semi-spherical nanoparticle, whether solid or hollow, can be elucidated through a straightforward analogy with Mie

theory [104].

When a nanobump emerges on the material surface, whether through localized growth or pushed by a deeper-formed nanocavity, the local electric field is locally intensified more prominently along the polarization of the field. Conversely, for a depression formed on the surface through cavitation or in the trough of a convection cell, given that the optical index of air is lower than that of the metal, the increased local field is mainly directed perpendicular to the polarization of the field. This constitutes the non-radiative electromagnetic response of the surface, contingent on the shape of the nanorelief.

This step of electromagnetic coupling in the near-field is of paramount importance for two reasons. Firstly,



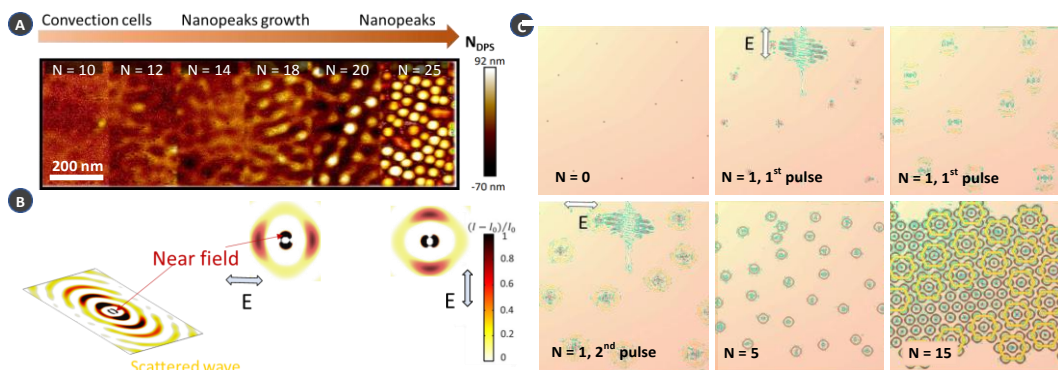


**FIGURE 11** A: Formation of convection prior to nanostructure growth, enhanced by feedback after several laser pulses for the Ni(001) material. B: Electromagnetic finite-difference time-domain simulation of near field scattering. C: Near field enhancement and formation of hexagonal convection cells at 15 pulses. Reproduced with permission [77, 56]. Copyright 2019, The Authors, De Gruyter publisher. Copyright 2022, The Authors, Wiley publisher.

it influences the orientation of energy deposition, inducing temperature gradient fields aligned with the polarization. The use of non-linearly polarized light or doubly polarized light in crossed directions, but not simultaneously, enables the orientation of temperature fields along two perpendicular axes.[105] Secondly, this step is crucial for the extension of the region affected by this non-radiative intensity, defined by the decay of the evanescent field. It is determined by the transverse absorption length, corresponding to the imaginary part of the optical index of the medium, and is of the same order of magnitude as the longitudinal optical depth, corresponding to the skin thickness. This is fundamental for achieving uniform energy confinement in all directions around the nanorelief, carrying significant implications for maintaining an optical feedback that is well balanced in both surface orientations. The field enhancement in this near-field range leads to energy localization, creating oriented thermal gradients. When considering the material's motion along this direction driven by the thermal gradients, thermocapillary migration in small-scale temperature gradients comes into play. This mechanism involves the temporal evolution of hydrodynamic and thermocapillary forces, determined by successive optical couplings in a multi-pulse regime. Under a single linear polarization, the emergence of 1D-LIPSS or HSFL

has been demonstrated through directed thermoconvection [46, 52, 53, 61]. Contrastingly, the variability of 2D-LIPSS morphology could depend on the level of anisotropy in the induced thermoconvection.

Early in the feedback process, near-field enhancement on local depression transforms into nanohexagons that self-organize into a hexagonal 2D lattice as presented in Figure 11 (B) and (C). This is due to hydrothermal flows guided by surface tension and rarefaction forces developing a thermoconvective instability at the nanoscale and, similarly to well-known Rayleigh-Bénard-Marangoni instabilities, generate convective cells as shown in Figure 11 (A) [52, 69]. The growth of the laser-induced structures from quasi-hexagonal cavities to uniform nanostructure is analyzed by combined electromagnetic and hydrodynamic approaches [52, 56, 79, 94].

## 5.2 | Convection and hydrodynamics instabilities

Self-organization regimes of 2D-LIPSS-II may result from complex flows occurring in the transiently laser-induced molten surface. At the considered fluence below ablation threshold, a thin liquid layer of 10-20 nm thickness is expected to be formed at the surface few

ps after irradiating a metal surface. During the first picosecond, an early thermomechanical excitation of the electrons occurs. During relaxation stage, the confined temperature gradient of femtosecond laser irradiation induces a pressure wave on the top surface which is followed by a rarefaction wave [60]. As a result, the melt layer is propelled towards the free surface by the rarefaction wave in the direction of the temperature gradient, as presented in Figure 12 (A). The normal force destabilizes the fluid interface, resulting in convection cells as illustrated by sequence of AFM images shown in Figure 11 (A). Similar to Rayleigh-Bénard convection, this entails the inverse destabilizing effect of gravitational force on a liquid heated from below [106].

Rarefaction forces are supplied by surface tension, while hydrothermal flows give rise to a thermoconvective instability at the nanoscale, akin to the established Rayleigh-Bénard-Marangoni instabilities. This mechanism represents a convincing scenario for generating hexagonal nanostructures (nanohexagons or nanohumps on the surface) [107]. The Rayleigh-Bénard-like instability arises due to a density gradient between the top and bottom surfaces. The rarefaction wave acts by pulling the cooler, denser liquid from the bottom to the top [108, 109]. Therefore, a Bénard-Marangoni convection occurs along the unstable fluids interface, initiated by small flow perturbations due to recurring surface tension gradients. This Marangoni flow transports thermal energy, that can be characterized by the Marangoni number, comparing the rate at which thermal energy is transported by this flow to the rate at which thermal energy diffuses. Modulated by near field coupling on local roughness sketched in Figure 11 (B-C), transverse temperature gradients are built parallel to the surface that turns to be unstable [69, 104].

Figure 12 (B) presents calculated surface dynamics upon ultrashort laser irradiation with a single pulse and horizontal polarization. The process is started by inhomogeneous energy absorption, followed by the presence of electromagnetic pattern at  $t = 10$  ps after electron-ion thermal equilibrium. Later on, at  $15$  ps  $< t < 25$  ps, the lattice density is strongly influenced by an inhomogeneous shock wave and rarefaction wave.

The destabilization occurs, the surface starts to melt inhomogeneously and the liquid flow is driven by transverse surface tension forces, rearranging the material from hot spots to colder regions on the surface [52]. Anisotropic temperature gradients generate hydrothermal waves and convection rolls in a disturbed thin liquid layer [110, 111]. This generates Marangoni forces balanced by thermal diffusion that reorganize the material over the surface into the most compact hexagonal way. Therefore, the dimensions and periods between cells are correlated to the Marangoni number which is equivalent the ratio between the destabilizing Marangoni force and the viscous restrictive force.

Moreover, Figure 12 (C) presents a height map of 2D-LIPSS-II observed on Ni (001) with respect to time-delay and laser fluence. In this map, the significant role of time delay in controlling the nanostructure height and type becomes noticeable. For example, at a fixed peak fluence of  $0.18 \text{ J/cm}^2$ , two different nanostructures can be obtained, the nanopikes at 8 ps and the nanohumps at 15 ps. These slight increments in time delay of a few ps have completely changed the aspect ratio, from 5 for nanopikes to almost 1 for nanohumps.

In order to understand the surface dynamics of double pulses and the significant role of time-delay, Figure 13 was established based on electromagnetic coupled with hydrodynamic simulation of Figure 12 (A) and (B), combined with experimental results.

For  $\Delta t \sim 8$  ps, 2D-LIPSS-II were observed with a height around 100 nm such as nanopikes and nanobumps, as presented in Figure 13 (A). However, for  $\Delta t \sim 15$  ps, 2D-LIPSS-II were observed with a height around 10 nm only, as presented in Figure 13 (B). In this Figure, the left arrow in red presents the first pulse timeline. The right timeline in blue presents the 2nd pulse, which has perpendicular polarization with the respect to the first pulse and delayed with a fixed time delay. For Figure 13 (A), the time delay was approximately 8 ps, whereas for Figure 13 (B), the time delay was approximately 15 ps.

For the first case, Figure 13 (A): the time delay is 8 ps, so the surface is still absorbing the first pulse when the second pulse reach the surface. At  $t = 15$  ps, the shock-

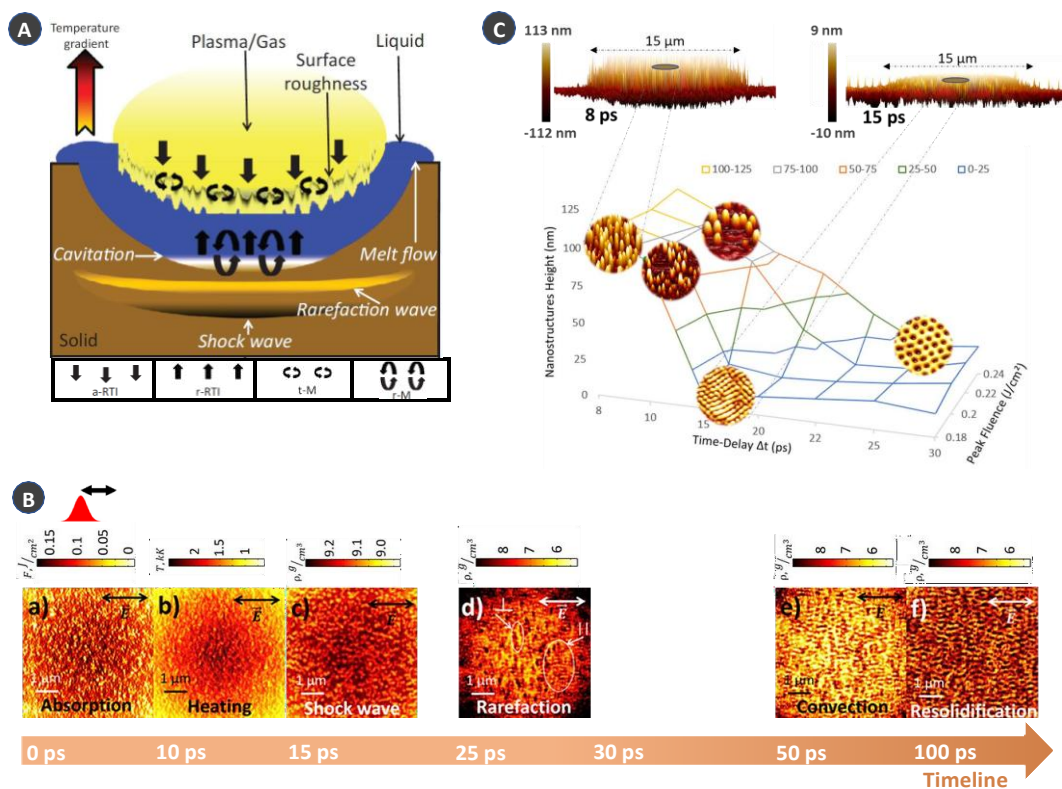


**FIGURE 12** A: Ultrashort-laser induced instabilities in a liquid layer: ablative Rayleigh-Taylor instability induced by recoil pressure (a-RTI), Marangoni convection instability (hydrothermal waves) induced by transverse temperature gradients on surface nanoroughness (t-M), Rayleigh-Taylor instability induced by rarefaction wave (r-RTI), Marangoni instability driven by rarefaction (r-M). Straight arrows indicate the direction of fluid flow acceleration, curved arrows show the direction of convection velocities. B: Surface dynamics upon ultrashort laser irradiation with peak fluence  $F = 0.5 \text{ J/cm}^2$  for a single pulse. (a) Absorbed energy on the initial surface, (b) maximum temperature distribution, and density snapshots (c-f) in the transverse plane are shown. C: Maximum nanostructure height as a function of time delay and laser fluence, illustrating nanopеaks reaching a maximum height of 113 nm compared to nanohumps with a maximum height of 9 nm for the Ni(001) material. Notably, the parameter responsible for the variation in nanostructure height is the increased time delay from 8 ps to 15 ps. Reproduced with permission [76, 52]. Copyright 2021, The Authors, MDPI publisher. Copyright 2020, The Authors, Elsevier publisher.

wave induced by the first pulse started to form, while the second pulse is heating the surface after absorption. At  $t = 24 \text{ ps}$ , the shockwave induced by the first pulse is intensifying while the second pulse shockwave has started, which create an amplified shockwave which lead to an amplified rarefaction wave and formation of high aspect ratio nanopеaks or nanobumps, depending on the laser fluence.

However, in the second scenario illustrated in Figure 13 (B), with  $\Delta t = 15 \text{ ps}$ , the shockwave induced by the first pulse had initiated by the time the second pulse reached the surface. At  $t = 25 \text{ ps}$ , the rarefaction caused by the shockwave of the first pulse had begun, concurrent with the initiation of the shockwave from the second pulse. This simultaneity resulted in minimized shockwave and rarefaction effects. Conse-

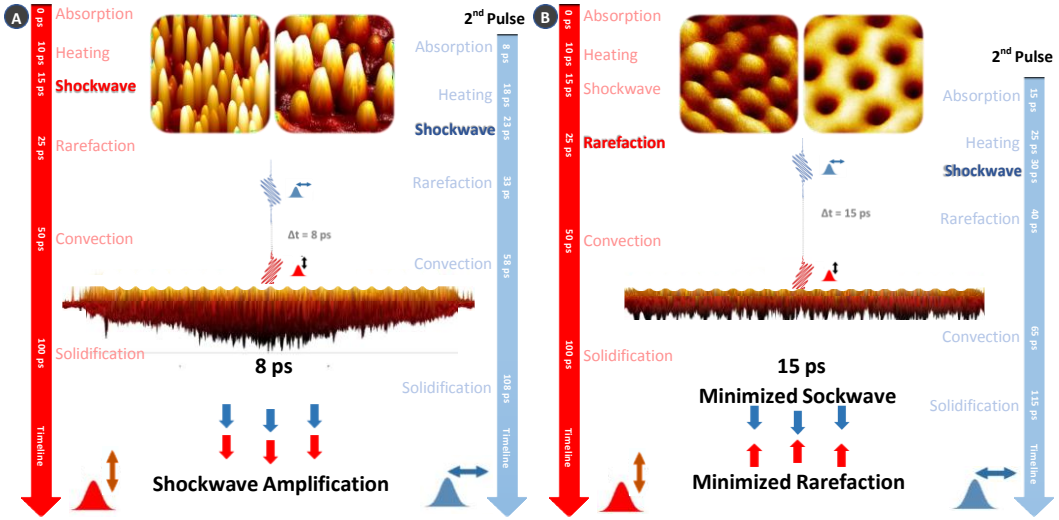


**FIGURE 13** A: schematic illustrating the influence of time delay on convection instabilities and their control over the type and aspect ratio of 2D-LIPSS-II. With a small  $\Delta t$  of 8 ps, the second pulse reaches a surface during the shockwave, intensifying it and amplifying the subsequent rarefaction. Conversely, at a higher  $\Delta t$  of 15 ps, the second pulse's shockwave reaches the surface during rarefaction, resulting in minimized rarefaction and the creation of organized nanostructures with smaller height. The material used in the figure is Ni(001).

quently, this extended time delay led to the formation of 2D-LIPSS-II with smaller height, such as nanohumps and nanohexagons, depending on the laser fluence.

Thus, the time delay plays a crucial role in fine-tuning the balance effects between the second shock wave and the first rarefaction wave. When comparing the height of nanostructures at a constant laser fluence of  $0.18 \text{ J/cm}^2$ , it becomes evident that at  $\Delta t = 8 \text{ ps}$ , the height of the nanostructures is 5 to 10 times greater than those at  $\Delta t = 15 \text{ ps}$ . This suggests that a smaller time delay can induce a more amplified shock wave, followed by a stronger rarefaction wave, resulting in longer nanostructures. On the other hand, a larger time delay can reduce the intensity of the shock wave.

## 6 | LIMITATIONS AND PERSPECTIVES

### 6.1 | Control the surface state for 2D-LIPSS-II

When dealing with manufacturing extremely small surface structures, especially ones on the scale of tens of nanometers, certain limitations come into play. These limitations become even more pronounced at such tiny scales. To explore this, let's turn our attention to Figure 14 (A). This visual guide highlights the fundamental importance of the initial surface's shape in the process of forming nanostructures. To achieve different surface shapes, various polishing methods have been proposed, resulting in surfaces with different levels of arithmetic average roughness (measured as  $R_a$ ). Upon close examination using an AFM scan covering an area of  $5 \times 5 \mu\text{m}^2$ , a critical revelation emerges—the value of  $R_a$  holds a pivotal role. Specifically, when  $R_a$  crosses the threshold of 5 nm ( $R_{a_{th}}$ ), it becomes a determining factor. Surface roughness beyond this threshold acts as a

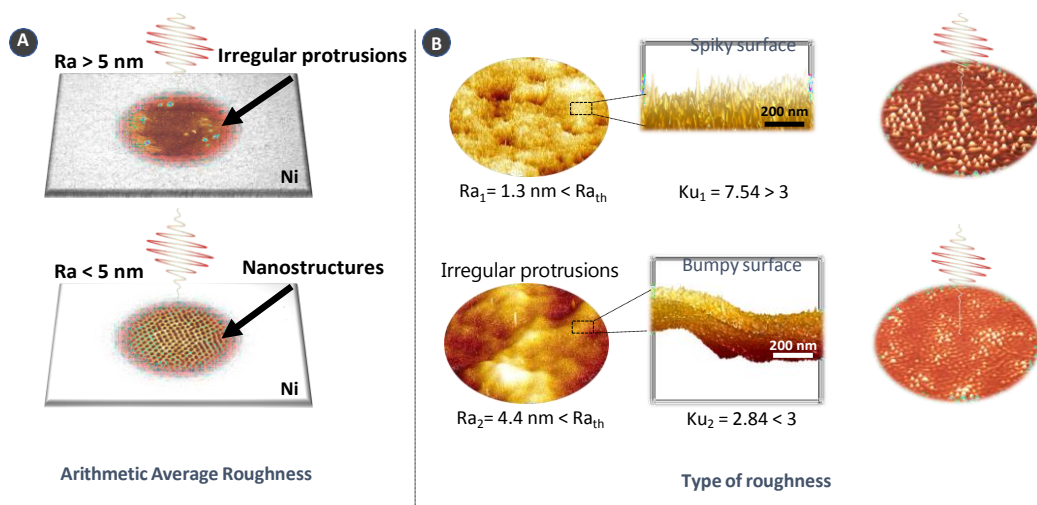


**FIGURE 14** A: Two different initial surface roughness values ( $R_a$ ) irradiated with the same laser parameters, highlighting the presence of an initial roughness threshold ( $R_{a_{th}}$ ) at approximately 5 nm. Beyond this threshold, the formation of 2D-LIPSS-II are unattainable. B: Initial surface topography of two distinct samples subjected to different polishing methods (mechanical polishing in (a) and electrochemical in (b)), both exhibiting  $R_a$  values less than  $R_{a_{th}}$ . Arithmetic roughness ( $R_a$ ) and Kurtosis ( $Ku$ ) were measured and compared for both samples. (c, d): 3D SEM images of samples (a) and (b) respectively after laser irradiation. The critical influence of the initial surface roughness type on nanostructure concentration is evident. The material used in the figure is Ni(001). Reproduced with permission [76]. Copyright 2021, The Authors, MDPI publisher.

barrier, preventing the creation of the previously mentioned nanohumps and nanohexagons that we've been exploring.

In Figure 14 (B), both mechanically and electrochemically polished samples exhibit initial roughness values below the defined  $R_{a_{th}}$ . Mechanical polishing involved a series of steps, including coarse paper up to P2400, followed by diamond polishing at 3  $\mu\text{m}$  and 1  $\mu\text{m}$ , and concluding with vibratory polishing using colloidal silica at 0.05  $\mu\text{m}$  for several hours. This meticulous process yielded a mirror-like surface with an exceptionally low arithmetic roughness. To assess the initial roughness and the sharpness of surface features, the Kurtosis ( $Ku$ ) statistical parameter was utilized. A  $Ku$  value exceeding 3 characterizes a "spiky" surface, while a value below 3 indicates a "bumpy" surface. When  $Ku$  equals 3, the surface exhibits entirely random roughness. The mechanically polished sample exhibits a  $Ku$  value of 7.54, classifying it as a spiky surface with an  $R_a$  below the

$R_{a_{th}}$  threshold. Conversely, the electrochemically polished sample was treated with stainless steel electrolyte at 25 Volts for 60 seconds. This process yielded an arithmetic roughness  $R_a$  of 4.4 nm, remaining below the  $R_{a_{th}}$  threshold. The  $Ku$  value for sample 2 is 2.84, signifying a bumpy surface.

Comparing the two textured surfaces under identical laser parameters clearly reveals differences in nanoparticle concentration. The spiky, mechanically polished surface is presumed to possess greater surface absorbance when contrasted with the bumpy, electrochemically polished surface. This dissimilarity in absorbance potentially contributes to the heightened concentration of nanostructures. It is noteworthy that the initial surface roughness type significantly influences both surface absorbance and reflectivity.

## 6.2 | Effects of polycrystalline states

The impact of crystalline orientation on the formation of 2D-LIPSS-II on polycrystalline nickel samples has been investigated [112]. The research sheds light on the uneven formation of structures on the surface of a metal when subjected to a low number of laser pulses. This non-uniform formation is attributed to the distinct responses of various crystalline orientations present on the surface.

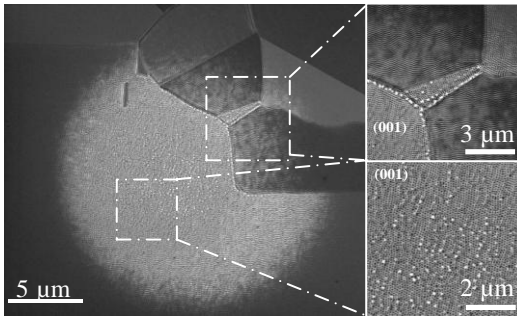


**FIGURE 15** SEM image of a site irradiated with 20 laser pulses at  $0.3 \text{ J/cm}^2$ . This clearly illustrate the competition between the formation of LIPSS and the accumulation of defects. The material used in this figure is a polycrystalline Ni. Reproduced with permission from [112] thesis. Copyright 2019.

Results obtained from the same irradiated nickel sample, as shown in Figure 15, demonstrate the discrepancy in structuring depending on the specific grain. Certain regions were magnified to discern the presence or absence of 2D-LIPSS-II, either within grains or near grain boundaries. This outcome underscores a pronounced orientation-dependent effect, with the (001) orientation exhibiting a higher propensity for the creation of nanohexagons on its surface. In essence, a competition arises between the absorbed laser energy's conversion into crystal defects and its transformation into periodic surface structures [113]. Moreover, this local crystal orientation subtly alters the threshold of the solid-liquid phase transition and influences the transient formation of surface roughness following the initial shots.

Moreover, irradiation of chromium (Cr) surfaces has

revealed that the material's response to the initial laser pulse is significantly influenced by its surface's crystallographic orientation. Specifically, the (001) surface of chromium demonstrates the creation of more extensive and refined nanoscale surface roughness compared to the (011) surface [24]. This heightened surface roughness resulting from the first laser pulse scatters laser light and induces local field enhancement upon exposure to the second laser pulse. Consequently, this phenomenon leads to the development of significantly more pronounced high spatial frequency structures on the (001) surface when compared to the (011) surface.

## 6.3 | How to reach the ultimate scale?

Reducing the laser wavelength presents an enticing avenue for further exploration. Previous studies have shown that a decrease in laser wavelength is linked to the generation of smaller structures in the context of LIPSS [114, 115]. In the domain of 2D-LIPSS, encompassing both types I and II, these questions remain intriguing and merit thorough investigation. Particularly, it is yet to be determined whether 2D-LIPSS-I could achieve a scale similar to that of 2D-LIPSS-II through laser wavelength reduction. Furthermore, delving into the limitations of 2D-LIPSS-II is of paramount interest - can even smaller scales be feasibly achieved? If so, what defines the boundary for this reduction? These inquiries delineate a stimulating path for future research, presenting opportunities to unravel novel phenomena at the nanoscale.

The formation of 2D-LIPSS necessitates that transverse temperature gradients ( $AT_T$ ) are of a similar magnitude to longitudinal temperature gradients ( $AT_L$ ). Typically,  $AT_L$  is determined by the optical skin depth, which is on the order of tens of nanometers for metals. High  $AT_L$  values, reaching up to  $\approx 10^{11} \text{ K m}^{-1}$ , result in a melted nanolayer and density changes in the fluid due to propagating shock waves. Transverse temperature gradients,  $AT_T$ , are driven by the extension of near-field absorption around surface roughness. This emphasizes the need to ensure that both the initial nanorelief structure (following the polishing process) and their transient

formation (after the first pulses) occur at the a scale comparable with the 3D-extent of optical absorption. Both  $AT_L$  and  $AT_T$  relax simultaneously, inducing oriented nanoscale effects. When these gradients act synergistically with a similar contribution, convective flows develop, and symmetry breaking nanopatterns can emerge due to the natural convection of irregular wavy structures on the surface. This emphasizes the criticality of confining electromagnetic fields to the smallest regions, specifically on the nanoreliefs, to enhance  $AT_L$  and  $AT_T$  for the successful generation of 2D-LIPSS at the ultimate scale.

#### 6.4 | Nonlinear dynamics modelling

The diverse range of characteristic shapes and sizes exhibited by LIPSS, notably resembling eolian sand dunes and structures observed during ion sputtering [64], has prompted the innovative notion of associating LIPSS with surface self-organization arising from a laser-induced surface instability [63]. This concept, well-established in explaining structure formation during ion sputtering, revolves around the central idea of structures forming due to a competition between surface roughening through erosion and surface smoothing through diffusion.

As previously presented for 2D-LIPSS-II, nanoscale fluid flows were shown to be driven by a complex interplay between electromagnetic, internal and surface pressure forces that can be trapped due to resolidification process. The prediction of underlying laser-coupling processes is constrained by a deterministic approach integrating low fluctuation conditions by surface roughness. Stationary patterns can become unstable under nonlinear amplification and bifurcate into more complex patterns that cannot be reliably described by classic approaches such as Navier-Stokes equations combined with Maxwell equations. Formally, convective instability patterns can be calculated by considering energetic fluctuation effects near the surface. Technically, introducing a noise term to the surface topography disrupts the uniform response of deterministic hydrodynamic equations by promoting strong inhomogeneous absorption. This

noise-induced perturbation leads to unexpected symmetries and chaos, providing a self-consistent framework for realistic laser-surface scenarios. To deepen the comprehension of complex dynamics in the presence of fluctuations during fluid instability onset, a recent advancement involves a nonlinear mathematical approach capable of predicting Turing-like patterns that lead to self-organization [93].

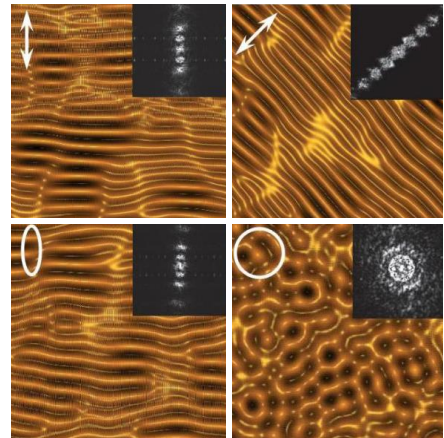


**FIGURE 16** Numerically calculated surfaces showing the surface morphologies with various parameters. The direction of incident electrical laser field is indicated with double arrows, ellipse and circle, correspondingly. The corresponding 2D-FFT images are presented in the inserts. Reproduced with permission [63]. Copyright 2011, Springer Science publisher.

The self-organization process was first proposed in the 1990s to theoretically explain a specific class of periodic laser-induced structures that differed qualitatively from LIPSS in that their orientation was unrelated to the laser polarization and the structure period was not directly correlated to the exciting radiation wavelength. Later, Reif et al. employed self-organization to explain the creation of LIPSS on wide bandgap materials using a nonlinear-dynamic erosion/smoothing model, based on Kuramoto-Sivashinsky equation commonly used in ion sputtering, to simulate surface patterning during multi-

pulse femtosecond laser ablation [63, 116, 117]:

$$\frac{\partial h}{\partial t} = -v(h) \left[ 1 + (Ah)^2 - KA^2(A^2h) \right] \quad (1)$$

where  $h$  corresponds to the growing surface profile.  $v$  and  $K$  are the erosion velocity and the self-diffusion term, respectively. It was demonstrated that the correlation of ripple topography and orientation with laser polarization can be characterized within a model in which the polarization creates an asymmetry in the deposited energy distribution and causes symmetry breaking on the surface. The model for dynamical systems generating spatio-temporally chaotic states has been adapted to account for how laser polarization affects nanostructure features can define directional anisotropy as presented in Figure 16.

In a similar manner but more tailored to thermoconvective flow, the Swift-Hohenberg (SH) model stands out as a powerful statistical model for understanding pattern formation in spatially extended systems which involve nonlocal interactions. Rooted in bifurcation theory and critical phenomena, the SH equation describes the emergence of diverse spatial patterns, such as stripes, spots, and hexagons, observed in experimental 2D LIPSS. Through spontaneous symmetry breaking and conservation laws, the model captures essential features of pattern dynamics, providing a statistical framework for analyzing the evolution of pattern amplitudes. The Swift-Hohenberg model was derived from a 2D projection of the governing fluid equations for Rayleigh-Bénard convection [118]. This projection, under the Boussinesq approximation, removes the dependence of the temperature, pressure, and velocity fields on the coordinate normal to the surface during hydrodynamic instabilities [118, 119]. SH approach, being a nonlinear dynamics model, is a favored choice for elucidating pattern formation phenomena owing to its simplicity, computational efficiency, emphasis on pattern formation, suitability for specific pattern systems, theoretical tractability, and versatility in capturing a diverse array of patterns. SH model incorporates nonlinearity terms that allow small amplitude destabilization, mimicking experimentally observed hexagonal patterns. With

its concise formulation, SH captures the essence of complex systems by manipulating precisely two key parameters to unveil a spectrum of emergent behaviors in convective processes. Its simplicity proves valuable, particularly in laser-surface interaction, where defining the out-of-equilibrium thermodynamic properties of the material (pressure, density, viscosity, surface tension, etc) can be challenging. Consequently, experimental patterns can be compared with specialized mathematical models tailored to describe the dynamics of nonlinear systems, facilitating a comprehensive exploration of the encompassed phase space.

Brandao et al. strategy relied on the use of Machine Learning (ML) integrating partial physical information in the form of the SH model to identify dominating stable modes for a set of parameters *independently* from initial roughness conditions [120]. This strategy enables to solve the dual inverse problem from a single observed state, consisting of an SEM image, with little data. This modelling is scale-invariant and can be applied to any laser process. It reduces experimental irradiation parameters to simple model coefficients, which can then be optimized and extrapolated for surface pattern engineering. The generalized Swift-Hohenberg equation was derived in an adimensional form as [93, 120]:

$$u' = \epsilon u - (1 + A^2)^2 u + \gamma u^2 - u^3. \quad (2)$$

Here,  $u$  is a real scalar field representing the surface amplitude, with  $x$ ,  $y$ , and  $t$  denoting spatial coordinates and time, respectively. The parameter  $\gamma$  refers to a symmetry-breaking factor driving the quadratic nonlinear term, enabling small-amplitude destabilization and the formation of hexagonal patterns as observed experimentally. The negative cubic term predominates for large amplitudes, controlling the magnitude of instabilities to limit the growth of the structures. Lastly,  $\epsilon > 0$  serves as the bifurcation parameter [121]. With appropriate boundary conditions, the original SH equation exhibits a type-I-s instability that is isotropic, invariant with respect to translations and to  $u \rightarrow -u$  [121]. Perturbations of  $u_b = 0$  are selectively amplified depending on the norm of the wavenumber, leading to the forma-



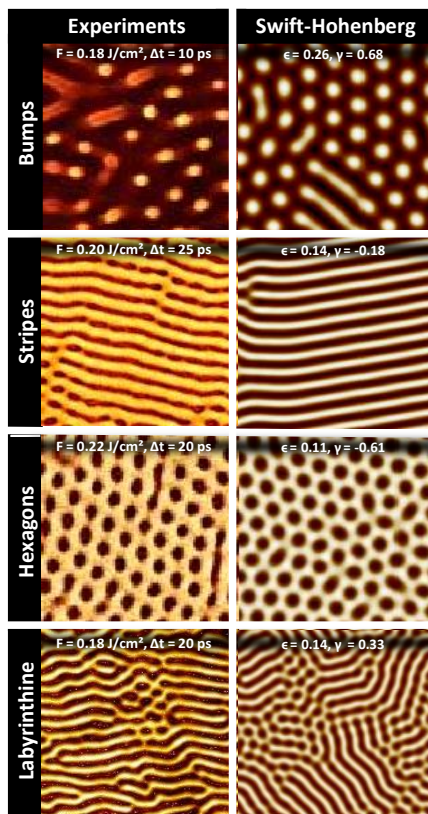


**FIGURE 17** SEM images were experimentally obtained under varied irradiation conditions to explore pattern regimes, along with the associated SH prediction for a specific set of  $(\epsilon, \gamma)$  parameters. The SH coefficients were derived using a pre-trained deep convolutional neural network approach, with permission [120]. Copyright 2023, The Authors, American Physical Society.

tion of complex *patterns* with no preferential direction.

Modifying the model coefficients, specifically adjusting the nonlinear strength and a bifurcation parameter that gauges the dimensionless proximity to the convection threshold in Rayleigh number terms, enables accurate replication of the nanostructures. Solutions resembling patterns in the SH equation closely resemble what we observe in the SEM images of irradiated surfaces, as depicted in Figure 17. In the presented results, a deep convolutional neural network approach was used to predict SH coefficients to generate solutions correspond-

ing to laser parameters unseen during training. This ML approach reduces experimental irradiation parameters to simple model coefficients, which can then be optimized and extrapolated for surface pattern engineering [93, 120].

## 7 | CONCLUSION

In summary, this comprehensive review explores the intricate transition from one-dimensional to two-dimensional LIPSS. Our primary focus is to comprehend this morphological evolution across diverse scales, shedding light on the fascinating domain of 2D structures. Through systematic categorization based on their periodicity, we reveal a remarkable array of configurations within 2D-LIPSS, all stemming from the fundamental mechanism of triggering fluid convection at varying scales. This categorization underscores the notable diversity inherent in these patterns of complexity.

Throughout this investigation, the intricacies of generating 2D-LIPSS-II structures at the finest scale have been explored, dissecting the critical parameters governing symmetry breaking and a morphological evolution of the patterns. These irradiation conditions, encompassing factors such as polarization and feedback have been meticulously examined, providing a profound understanding of the subtle interplay between the features of scattered light and matter reorganization at the nanoscale.

Theoretical investigations have highlighted the key role of convective flows triggered by polarization-dependent photoexcitation as primary mechanisms shaping these captivating symmetries. The issue of pattern reproducibility is at the core of self-organized processes. In particular, initial conditions, such as surface roughness properties or local effects of crystallographic orientations, must be meticulously controlled. The selection and preparation of the surface prior to irradiation are as crucial as the laser parameters in governing the process.

In a broader sense, instead of merely following one af-

ter another, the profound influence of preferential light orientations on surface features and self-organization can be intricately interconnected, unveiling several patterns simultaneously. The interplay among these overlapping patterning processes significantly contributes to achieve a stable and replicable pattern. This suggests that 2D surface self-organization is elaborated in a non-localized manner within the laser impact zone, presenting opportunities for uniform and coherent structuring during impact superposition.

The precision and resilience observed in the development of nanostructures, once seen as random or speculative, can now be meticulously quantified through experimental endeavors. Moreover, within a framework of nonlinear dynamical systems tailored for dissipative structures, machine learning provides a powerful tool to analyze pattern expression variability and predict conditions to extrapolate towards yet-to-be-observed patterns. This opens doors to potential applications across a wide spectrum of nanoscience domains, including nanophotonics, nanofluidics, and nanocatalysis, charting a promising trajectory toward impactful advancements.

## Aknowledgments

The authors would like to express their gratitude to C. Maurice, F. Garrelie, A. Rudenko, E. Brandao and F. Pigeon for their valuable support and insightful discussions, which greatly enriched the content of this review.

## Conflict of Interest

The authors declare no conflict of interest.

## references

- [1] Lal S, Link S, Halas NJ. Nano-optics from sensing to waveguiding. *Nat Photonics* 2007 Nov;1:641-648.
- [2] Fitriani, Ovik R, Long BD, Barma MC, Riaz M, Sabri MFM, et al. A review on nanostructures of high-temperature thermoelectric materials for waste heat recovery. *Renewable Sustainable Energy Rev* 2016 Oct;64:635-659.
- [3] Chen X, Zhang L. Review in manufacturing methods of nanochannels of bio-nanofluidic chips. *Sens Actuators, B* 2018 Jan;254:648-659.
- [4] Malinauskas M, Žukauskas A, Hasegawa S, Hayasaki Y, Mizeikis V, Buividas R, et al. Ultrafast laser processing of materials: from science to industry. *Light: Science & Applications* 2016;5(8):e16133-e16133.
- [5] Stoian R, Colombier JP. Advances in ultrafast laser structuring of materials at the nanoscale. *Nanophotonics* 2020;9(16):4665-4688.
- [6] Birnbaum M. Semiconductor surface damage produced by ruby lasers. *J Appl Phys* 1965;36(11):3688-3689.
- [7] Strickland D, Mourou G. Compression of amplified chirped optical pulses. *Opt Commun* 1985 Oct;55(6):447-449.
- [8] Gao YF, Yu CY, Han B, Ehrhardt M, Lorenz P, Xu LF, et al. Picosecond laser-induced periodic surface structures (LIPSS) on crystalline silicon. *Surf Interfaces* 2020 Jun;19:100538.
- [9] Zhang H, Colombier JP, Witte S. Laser-induced periodic surface structures: Arbitrary angles of incidence and polarization states. *Physical Review B* 2020;101(24):245430.
- [10] Borowiec A, Haugen HK. Subwavelength ripple formation on the surfaces of compound semiconductors irradiated with femtosecond laser pulses. *Appl Phys Lett* 2003 Jun;82(25):4462-4464.
- [11] Le Harzic R, Stracke F, Zimmermann H. Formation mechanism of femtosecond laser-induced high spatial frequency ripples on semiconductors at low fluence and high repetition rate. *J Appl Phys* 2013 May;113(18).
- [12] Senegačnik M, Hočevár M, Gregorčič P. Influence of processing parameters on characteristics of laser-induced periodic surface structures on steel and titanium. *Procedia CIRP* 2019;81:99-103.
- [13] Bonse J, Krüger J, Höhm S, Rosenfeld A. Femtosecond laser-induced periodic surface structures. *J Laser Appl* 2012 Jul;24(4):042006.
- [14] Vorobyev AY, Guo C. Direct femtosecond laser surface nano / microstructuring and its applications. *Laser Photonics Rev* 2013 May;7(3):385-407.

- [15] Gnilitzky I, Derrien TJY, Levy Y, Bulgakova NM, Orazi L. High-speed manufacturing of highly regular femtosecond laser-induced periodic surface structures: Physical origin of regularity. *Sci Rep* 2017 Aug;7(1).
- [16] Prudent M, Bourquard F, Borroto A, Pierson JF, Garrelie F, Colombier JP. Initial morphology and feedback effects on laser-induced periodic nanostructuring of thin-film metallic glasses. *Nanomaterials* 2021;11(5):1076.
- [17] Garcia-Lechuga M, Puerto D, Fuentes-Edfuf Y, Solis J, Siegel J. Ultrafast moving-spot microscopy: Birth and growth of laser-induced periodic surface structures. *Acs Photonics* 2016;3(10):1961-1967.
- [18] Mastellone M, Pace ML, Curcio M, Caggiano N, De Bonis A, Teghil R, et al. LIPSS Applied to Wide Bandgap Semiconductors and Dielectrics: Assessment and Future Perspectives. *Materials* 2022 Feb;15(4):1378.
- [19] Heitz J, Reisinger B, Fahrner M, Romanin C, Siegel J, Svorcik V. Laser-induced periodic surface structures (LIPSS) on polymer surfaces. In: 2012 14th International Conference on Transparent Optical Networks (ICTON) IEEE; p. 02-05.
- [20] Dorransoro C, Siegel J, Remon L, Marcos S. Suitability of Filofocon A and PMMA for experimental models in excimer laser ablation refractive surgery. *Optics Express* 2008;16(25):20955-20967.
- [21] Rebollar E, Castillejo M, Ezquerro TA. Laser induced periodic surface structures on polymer films: From fundamentals to applications. *Eur Polym J* 2015 Dec;73:162-174.
- [22] Gnilitzky I, Alnusirat W, Sorgato M, Orazi L, Lucchetta G. Effects of anisotropic and isotropic LIPSS on polymer filling flow and wettability of micro injection molded parts. *Opt Laser Technol* 2023 Feb;158:108795.
- [23] Bonse J, Koter R, Hartelt M, Spaltmann D, Pentzien S, Höhm S, et al. Tribological performance of femtosecond laser-induced periodic surface structures on titanium and a high toughness bearing steel. *Appl Surf Sci* 2015;336:21-27.
- [24] Abou-Saleh A, Karim ET, Maurice C, Reynaud S, Pigeon F, Garrelie F, et al. Spallation-induced roughness promoting high spatial frequency nanostructure formation on Cr. *Appl Phys A: Mater Sci Process* 2018 Apr;124(4):308.
- [25] Wang J, Guo C. Ultrafast dynamics of femtosecond laser-induced periodic surface pattern formation on metals. *Appl Phys Lett* 2005 Dec;87(25):251914.
- [26] Colombier JP, Garrelie F, Faure N, Reynaud S, Bounhalli M, Audouard E, et al. Effects of electron-phonon coupling and electron diffusion on ripples growth on ultrafast-laser-irradiated metals. *J Appl Phys* 2012 Jan;111(2):024902.
- [27] Höhm S, Rohloff M, Krüger J, Bonse J, Rosenfeld A. Formation of Laser-Induced Periodic Surface Structures (LIPSS) on Dielectrics and Semiconductors upon Double-Femtosecond Laser Pulse Irradiation Sequences. In: *Progress in Nonlinear Nano-Optics* Springer; 2014.p. 85-99.
- [28] Dusser B, Sagan Z, Soder H, Faure N, Colombier JP, Jourlin M, et al. Controlled nanostructures formation by ultra fast laser pulses for color marking. *Opt Express* 2010 Feb;18(3):2913-2924.
- [29] Vorobyev AY, Guo C. Coloring metals with femtosecond laser pulses. *Appl Phys Lett* 2008 Jan;92(4):041914.
- [30] Guay JM, Lesina AC, Côté G, Charron M, Weck A. Laser-induced plasmonic colours on metals. *Nat Commun* 2017 Jul;8(1):16095.
- [31] Qiao M, Yan J, Jiang L. Direction Controllable Nanopatterning of Titanium by Ultrafast Laser for Surface Coloring and Optical Encryption. *Adv Opt Mater* 2022 Feb;10(3):2101673.
- [32] Wang Z, Zhao Q, Wang C. Reduction of Friction of Metals Using Laser-Induced Periodic Surface Nanostructures. *Micromachines* 2015 Oct;6(11):1606-1616.
- [33] Wang Z, Zhao QZ. Friction reduction of steel by laser-induced periodic surface nanostructures with atomic layer deposited TiO<sub>2</sub> coating. *Surf Coat Technol* 2018 Jun;344:269-275.
- [34] Kunz C, Bonse J, Spaltmann D, Neumann C, Turchanian A, Bartolomé JF, et al. Tribological performance of metal-reinforced ceramic composites selectively structured with femtosecond laser-induced periodic surface structures. *Appl Surf Sci* 2020 Jan;499:143917.
- [35] Stratakis E, Bonse J, Heitz J, Siegel J, Tsididis GD, Skoulas E, et al. Laser engineering of biomimetic surfaces. *Materials Science and Engineering: R: Reports* 2020 Jul;141:100562.

- [36] Yao C, Ye Y, Jia B, Li Y, Ding R, Jiang Y, et al. Polarization and fluence effects in femtosecond laser induced micro/nano structures on stainless steel with antireflection property. *Appl Surf Sci* 2017 Dec;425:1118-1124.
- [37] Wang H, Zhang F, Yin K, Duan J. Bioinspired antireflective subwavelength nanostructures induced by femtosecond laser for high transparency glass. *J Non-Cryst Solids* 2023 Jan;600:122016.
- [38] Raimbault O, Benayoun S, Anselme K, Mauclair C, Bourgade T, Kietzig AM, et al. The effects of femtosecond laser-textured Ti-6Al-4V on wettability and cell response. *Mater Sci Eng, C* 2016 Dec;69:311-320.
- [39] Orazi L, Gniliyskiy I, Serro AP. Laser Nanopatterning for Wettability Applications. *J Micro Nano-Manuf* 2017 Jun;5(2):21008.
- [40] Khorkov KS, Kochuev DA, Dzus MA, Prokoshev VG. Wettability surface control on stainless steel by LIPSS formation. *J Phys Conf Ser* 2021 Feb;1822(1):012010.
- [41] Du C, Wang C, Zhang T, Zheng L. Antibacterial Performance of Zr-BMG, Stainless Steel, and Titanium Alloy with Laser-Induced Periodic Surface Structures. *ACS Appl Bio Mater* 2022 Jan;5(1):272-284.
- [42] Erkızan SN, İdikut F, Demirtaş Ö, Goodarzi A, Demir AK, Borra M, et al. LIPSS for SERS: Metal Coated Direct Laser Written Periodic Nanostructures for Surface Enhanced Raman Spectroscopy. *Adv Opt Mater* 2022 Nov;10(22):2200233.
- [43] Liu YH, Yeh SC, Cheng CW. Two-dimensional periodic nanostructure fabricated on titanium by femtosecond green laser. *Nanomaterials* 2020;10(9):1820.
- [44] Colombier JP, Rudenko A, Silaeva E, Zhang H, Sedao X, Bévilion E, et al. Mixing periodic topographies and structural patterns on silicon surfaces mediated by ultrafast photoexcited charge carriers. *Physical Review Research* 2020;2(4):043080.
- [45] Becher MJMJ, Jagosz J, Bock C, Ostendorf A, Gurevich EL. Formation of low and high spatial frequency laser-induced periodic surface structures (LIPSS) in ALD deposited MoS<sub>2</sub>. *Frontiers in Nanotechnology*;5:1227025.
- [46] Kawabata S, Bai S, Obata K, Miyaji G, Sugioka K. Two-dimensional laser-induced periodic surface structures formed on crystalline silicon by GHz burst mode femtosecond laser pulses. *International Journal of Extreme Manufacturing* 2023;5(1):015004.
- [47] Van Driel H, Sipe J, Young JF. Laser-induced periodic surface structure on solids: A universal phenomenon. *Physical Review Letters* 1982;49(26):1955.
- [48] Buividas R, Mikutis M, Juodkazis S. Surface and bulk structuring of materials by ripples with long and short laser pulses: Recent advances. *Progress in Quantum Electronics* 2014;38(3):119-156.
- [49] Tsididis GD, Skoulas E, Papadopoulos A, Stratakis E. Convection roll-driven generation of supra-wavelength periodic surface structures on dielectrics upon irradiation with femtosecond pulsed lasers. *Physical Review B* 2016;94(8):081305.
- [50] Sun H, Li J, Liu M, Yang D, Li F. A review of effects of femtosecond laser parameters on metal surface properties. *Coatings* 2022;12(10):1596.
- [51] Tsididis GD, Fotakis C, Stratakis E. From ripples to spikes: A hydrodynamical mechanism to interpret femtosecond laser-induced self-assembled structures. *Physical Review B* 2015;92(4):041405.
- [52] Rudenko A, Abou-Saleh A, Pigeon F, Mauclair C, Garrelie F, Stoian R, et al. High-frequency periodic patterns driven by non-radiative fields coupled with Marangoni convection instabilities on laser-excited metal surfaces. *Acta Materialia* 2020;194:93-105.
- [53] Bonse J, Gräf S. Maxwell Meets Marangoni—A Review of Theories on Laser-Induced Periodic Surface Structures. *Laser & Photonics Reviews* 2020;14(10):2000215.
- [54] Rudenko A, Colombier JP. How light drives material periodic patterns down to the nanoscale. In: *Ultrafast Laser Nanostructuring: The Pursuit of Extreme Scales* Springer; 2023.p. 209-255.
- [55] Kuzmin E, Polyakov D, Samokhvalov A, Shandybina G. Cylindrical and plane surface electromagnetic waves in laser technology of silicon surface texturing with a double femtosecond pulse. *Optical and Quantum Electronics* 2019;51:1-10.
- [56] Rudenko A, Mauclair C, Garrelie F, Stoian R, Colombier JP. Self-organization of surfaces on the nanoscale by topography-mediated selection of

- quasi-cylindrical and plasmonic waves. *Nanophotonics* 2019;8(3):459-465.
- [57] Kravets VG, Kabashin AV, Barnes WL, Grigorenko AN. Plasmonic surface lattice resonances: a review of properties and applications. *Chemical Reviews* 2018;118(12):5912-5951.
- [58] Sokolowski-Tinten K, Bonse J, Barty A, Chapman HN, Bajt S, Bogan MJ, et al. In-situ observation of the formation of laser-induced periodic surface structures with extreme spatial and temporal resolution. In: *Ultrafast Laser Nanostructuring: The Pursuit of Extreme Scales* Springer; 2023.p. 257-276.
- [59] Terekhin PN, Oltmanns J, Blumenstein A, Ivanov DS, Kleinwort F, Garcia ME, et al. Key role of surface plasmon polaritons in generation of periodic surface structures following single-pulse laser irradiation of a gold step edge. *Nanophotonics* 2021;11(2):359-367.
- [60] Sedao X, Abou Saleh A, Rudenko A, Douillard T, Esnouf C, Reynaud S, et al. Self-Arranged Periodic Nanovoids by Ultrafast Laser-Induced Near-Field Enhancement. *ACS Photonics* 2018 Apr;5(4):1418-1426.
- [61] Zhang D, Liu R, Li Z. Irregular LIPSS produced on metals by single linearly polarized femtosecond laser. *International Journal of Extreme Manufacturing* 2021;4(1):015102.
- [62] Emel'yanov V. Kuramoto–Sivashinsky equation for modulation of surface relief of molten layer and formation of surface periodic microstructures under pulsed laser irradiation of solids. *Laser Physics* 2011;21:222-228.
- [63] Reif J, Varlamova O, Varlamov S, Bestehorn M. The role of asymmetric excitation in self-organized nanostructure formation upon femtosecond laser ablation. *AIP Conf Proc* 2012 Jul;1464(1):428-441.
- [64] Bradley RM, Harper JM. Theory of ripple topography induced by ion bombardment. *Journal of Vacuum Science & Technology A: Vacuum, Surfaces, and Films* 1988;6(4):2390-2395.
- [65] Castro M, Cuerno R, Vázquez L, Gago R. Self-organized ordering of nanostructures produced by ion-beam sputtering. *Physical Review Letters* 2005;94(1):016102.
- [66] Bradley RM. Theory of nanoscale ripple topographies produced by ion bombardment near the threshold for pattern formation. *Physical Review E* 2020;102(1):012807.
- [67] Son JG, Choi JW, Seo O, Noh DY, Ko DK. Morphology evolution of self-organized porous structures in silicon surface. *Results in Physics* 2019;12:46-51. <https://www.sciencedirect.com/science/article/pii/S2211379718327426>.
- [68] Durbach S, Krauss FT, Hoffmann M, Lehmann V, Reinhardt H, Sundermeyer J, et al. Laser-Driven One- and Two-Dimensional Subwavelength Periodic Patterning of Thin Films Made of a Metal-Organic MoS<sub>2</sub> Precursor. *ACS Nano* 2022 Jul;16(7):10412-10421.
- [69] Abou Saleh A, Rudenko A, Reynaud S, Pigeon F, Garrelie F, Colombier JP. Sub-100 nm 2D nanopatterning on a large scale by ultrafast laser energy regulation. *Nanoscale* 2020;12(12):6609-6616.
- [70] Romano JM, Helbig R, Fraggelakis F, Garcia-Giron A, Werner C, Kling R, et al. Springtail-Inspired Triangular Laser-Induced Surface Textures on Metals Using MHz Ultrashort Pulses. *J Micro Nano-Manuf* 2019 Jun;7(2):024504.
- [71] Liu W, Sun J, Hu J, Jiang L, Huang J, Li Z, et al. Transformation from nano-ripples to nano-triangle arrays and their orientation control on titanium surfaces by using orthogonally polarized femtosecond laser double-pulse sequences. *Appl Surf Sci* 2022 Jun;588:152918.
- [72] Jalil SA, Yang J, Elkabbash M, Cong C, Guo C. Formation of controllable 1D and 2D periodic surface structures on cobalt by femtosecond double pulse laser irradiation. *Appl Phys Lett* 2019 Jul;115(3):031601.
- [73] Giannuzzi G, Gaudio C, Di Mundo R, Mirengi L, Fraggelakis F, Kling R, et al. Short and long term surface chemistry and wetting behaviour of stainless steel with 1D and 2D periodic structures induced by bursts of femtosecond laser pulses. *Appl Surf Sci* 2019 Nov;494:1055-1065.
- [74] Nakhoul A. Surface morphology control at the nanoscale by temporal and polarization control of ultrafast laser pulses. PhD thesis, Université Jean Monnet - Saint-Etienne; 2022.
- [75] Nakhoul A, Maurice C, Faure N, Garrelie F, Pigeon F, Colombier JP. Tailoring the surface morphology of Ni at the nanometric scale by ultrashort laser pulses. *Appl Phys A* 2022 Oct;128(10):1-7.

- [76] Nakhoul A, Maurice C, Agoyan M, Rudenko A, Garrelie F, Pigeon F, et al. Self-Organization Regimes Induced by Ultrafast Laser on Surfaces in the Tens of Nanometer Scales. *Nanomaterials* 2021;11(4):1020.
- [77] Nakhoul A, Rudenko A, Maurice C, Reynaud S, Garrelie F, Pigeon F, et al. Boosted Spontaneous Formation of High-Aspect Ratio Nanopeaks on Ultrafast Laser-Irradiated Ni Surface. *Adv Sci* 2022 Jul;9(21):2200761.
- [78] Zhang H, Colombier JP, Li C, Faure N, Cheng G, Stoian R. Coherence in ultrafast laser-induced periodic surface structures. *Phys Rev B* 2015 Nov;92(17):174109.
- [79] Rudenko A, Colombier JP, Höhm S, Rosenfeld A, Krüger J, Bonse J, et al. Spontaneous periodic ordering on the surface and in the bulk of dielectrics irradiated by ultrafast laser: a shared electromagnetic origin. *Sci Rep* 2017 Sep;7(12306):1-14.
- [80] Bonse J, Kirner SV, Griepentrog M, Spaltmann D, Krüger J. Femtosecond Laser Texturing of Surfaces for Tribological Applications. *Materials* 2018 May;11(5):801.
- [81] Kawakami Y, Ozawa E, Sasaki S. Coherent array of tungsten ultrafine particles by laser irradiation. *Appl Phys Lett* 1999 Jun;74(26):3954-3956.
- [82] van der Poel SH, Mezera M, Römer GWRBE, de Vries EG, Matthews DTA. Fabricating Laser-Induced Periodic Surface Structures on Medical Grade Cobalt-Chrome-Molybdenum: Tribological, Wetting and Leaching Properties. *Lubricants* 2019 Aug;7(8):70.
- [83] Romano JM, Garcia-Giron A, Penchev P, Dimov S. Triangular laser-induced submicron textures for functionalising stainless steel surfaces. *Appl Surf Sci* 2018 Jan;440:162-169.
- [84] Fraggelakis F, Mincuzzi G, Lopez J, Manek-Hönninger I, Kling R. Controlling 2D laser nano structuring over large area with double femtosecond pulses. *Appl Surf Sci* 2019 Mar;470:677-686.
- [85] Fraggelakis F, Mincuzzi G, Lopez J, Kling R, Manek-Hönninger I. Controlling Micron and Submicron Scale Laser Induced Surface Structures on Stainless Steel with Industrial Femtosecond Lasers. *Journal of Laser Micro / Nanoengineering* 2018 Dec;13(3):206-210.
- [86] Porta-Velilla L, Turan N, Cubero Á, Shao W, Li H, de la Fuente GF, et al. Highly Regular Hexagonally-Arranged Nanostructures on Ni-W Alloy Tapes upon Irradiation with Ultrashort UV Laser Pulses. *Nanomaterials* 2022 Jul;12(14):2380.
- [87] Mastellone M, Bellucci A, Girolami M, Serpente V, Polini R, Orlando S, et al. Deep-Subwavelength 2D Periodic Surface Nanostructures on Diamond by Double-Pulse Femtosecond Laser Irradiation. *Nano Lett* 2021 May;21(10):4477-4483.
- [88] Hoehm S, Rosenfeld A, Krueger J, Bonse J. Femtosecond laser-induced periodic surface structures on silica. *J Appl Phys* 2012 Jul;112(1):014901.
- [89] Nivas JJJ, Amoroso S. Generation of Supra-Wavelength Grooves in Femtosecond Laser Surface Structuring of Silicon. *Nanomaterials* 2021 Jan;11(1):174.
- [90] Her TH, Finlay RJ, Wu C, Mazur E. Femtosecond laser-induced formation of spikes on silicon. *Appl Phys A* 2000 Apr;70(4):383-385.
- [91] Kawakami Y, Ozawa E. Self-assembled coherent array of ultra-fine particles on single-crystal tungsten substrate using SHG Nd:YAG laser. *Appl Phys A: Mater Sci Process* 2000 Oct;71(4):453-456.
- [92] Nakhoul A, Rudenko A, Sedao X, Peillon N, Colombier JP, Maurice C, et al. Energy feedthrough and microstructure evolution during direct laser peening of aluminum in femtosecond and picosecond regimes. *J Appl Phys* 2021 Jul;130(1):015104.
- [93] Brandao E, Colombier JP, Dufner S, Emonet R, Garrelie F, Habrard A, et al. Learning PDE to Model Self-Organization of Matter. *Entropy (Basel)* 2022 Aug;24(8):1096.
- [94] Tsidis GD, Fotakis C, Stratakis E. From ripples to spikes: A hydrodynamical mechanism to interpret femtosecond laser-induced self-assembled structures. *Phys Rev B* 2015 Jul;92(4):041405.
- [95] Kawakami Y, Ozawa E. Tungsten microcone growth by laser irradiation. *Appl Surf Sci* 2003 Sep;218(1):176-188.
- [96] Fraggelakis F, Mincuzzi G, Lopez J, Manek-Hönninger I, Kling R. 2D laser induced periodic surface structures with double cross-polarized pulses. In: *Proceedings Volume 10520, Laser-based Micro- and Nanoprocessing XII*, vol. 10520 SPIE; 2018.p. 98-105.

- [97] Busse FH, Whitehead JA. Instabilities of convection rolls in a high Prandtl number fluid. *J Fluid Mech* 1971 May;47(2):305-320.
- [98] Bévillon E, Stoian R, Colombier JP. Nonequilibrium optical properties of transition metals upon ultrafast electron heating. *J Phys: Condens Matter* 2018 Aug;30(38):385401.
- [99] Echebarria B, Riecke H. Defect chaos of oscillating hexagons in rotating convection. *Physical review letters* 2000;84(21):4838.
- [100] Guo T, Han K, Heng L, Cao M, Jiang L. Ordered porous structure hybrid films generated by breath figures for directional water penetration. *RSC Adv* 2015 Oct;5(107):88471-88476.
- [101] Zhang A, Bai H, Li L. Breath Figure: A Nature-Inspired Preparation Method for Ordered Porous Films. *Chem Rev* 2015 Sep;115(18):9801-9868.
- [102] Zhigilei LV, Kodali PBS, Garrison BJ. Molecular Dynamics Model for Laser Ablation and Desorption of Organic Solids. *J Phys Chem B* 1997 Mar;101(11):2028-2037.
- [103] Shugaev MV, He M, Levy Y, Mazzi A, Miotello A, Bulgakova NM, et al. Laser-induced thermal processes: heat transfer, generation of stresses, melting and solidification, vaporization, and phase explosion. In: *Handbook of Laser Micro-and Nano-Engineering* Springer; 2021.p. 83-163.
- [104] Rudenko A, Maclair C, Garrelie F, Stoian R, Colombier JP. Light absorption by surface nanoholes and nanobumps. *Appl Surf Sci* 2019 Mar;470:228-233.
- [105] Abou Saleh A, Rudenko A, Douillard L, Pigeon F, Garrelie F, Colombier JP. Nanoscale imaging of ultrafast light coupling to self-organized nanostructures. *ACS photonics* 2019;6(9):2287-2294.
- [106] Bodenschatz E, Pesch W, Ahlers G. Recent Developments in Rayleigh-Bénard Convection. *Annu Rev Fluid Mech* 2000 Jan;32(1):709-778.
- [107] Thess A, Bestehorn M. Planform selection in Bénard-Marangoni convection: Hexagons versus g hexagons. *Phys Rev E* 1995 Dec;52(6):6358-6367.
- [108] Sharp DH. An overview of Rayleigh-Taylor instability. *Physica D* 1984 Jul;12(1):3-18.
- [109] Morgan RV, Cabot WH, Greenough JA, Jacobs JW. Rarefaction-driven Rayleigh-Taylor instability. Part 2. Experiments and simulations in the nonlinear regime. *J Fluid Mech* 2018 Mar;838:320-355.
- [110] Smith MK, Davis SH. Instabilities of dynamic thermocapillary liquid layers. Part 1. Convective instabilities. *J Fluid Mech* 1983 Jul;132:119-144.
- [111] Smith MK. Instability mechanisms in dynamic thermocapillary liquid layers. *Phys Fluids* 1986 Oct;29(10):3182-3186.
- [112] Saleh AA. Relation entre auto-organisation et création/résorption de défauts microstructuraux sous irradiation laser ultrabrèves. PhD thesis, Université de Lyon; 2019.
- [113] Sedao X, Maurice C, Garrelie F, Colombier JP, Reynaud S, Quey R, et al. Influence of crystal orientation on the formation of femtosecond laser-induced periodic surface structures and lattice defects accumulation. *Appl Phys Lett* 2014 Apr;104(17):171605.
- [114] Pallarés-Aldeiturriaga D, Papa S, Abou Khalil A, Pascale-Hamri A, Maalouf M, Di Maio Y, et al. Influence of multi-wavelength ultrafast laser texturing and autoclave sterilization on titanium alloy-based surface wettability. *Appl Phys A* 2022 Oct;128(10):1-5.
- [115] Khalil AA, Papa S, Compère N, Hamri AP, Guignandon A, Dumas V, et al. Multi-wavelength femtosecond laser LIPSS generation on titanium alloy and comparative study of their effect on cell adhesions. In: *Proceedings Volume PC11991, Frontiers in Ultrafast Optics: Biomedical, Scientific, and Industrial Applications XXII*, vol. PC11991 SPIE; 2022.p. PC1199108.
- [116] Varlamova O, Bounhalli M, Reif J. Influence of irradiation dose on laser-induced surface nanostructures on silicon. *Appl Surf Sci* 2013 Aug;278:62-66.
- [117] Costache F, Henyk M, Reif J. Modification of dielectric surfaces with ultra-short laser pulses. *Appl Surf Sci* 2002 Jan;186(1):352-357.
- [118] Swift J, Hohenberg PC. Hydrodynamic fluctuations at the convective instability. *Physical Review A* 1977;15(1):319.
- [119] Chandrasekhar S. *Hydrodynamic and hydromagnetic stability*. Courier Corporation; 2013.

- [120] Brandao E, Nakhoul A, Duñher S, Emonet R, Garrelie F, Habrard A, et al. Learning Complexity to Guide Light-Induced Self-Organized Nanopatterns. *Physical Review Letters* 2023;130(22):226201.
- [121] Cross MC, Hohenberg PC. Pattern formation outside of equilibrium. *Rev Mod Phys* 1993 Jul;65(3):851-1112.